

Exploring the Origin of Geoid Low and Topography High in West Antarctica: Insights from Density Anomalies and Mantle Convection Models

Bernhard Steinberger *^{1,2}, Maya-Lauren Grasnick ³, Ronja Ludwig ⁴

¹GFZ German Research Centre for Geosciences, Telegrafenberg, 5 14473 Potsdam, Germany | ²Centre for Earth Evolution and Dynamics, University of Oslo, PO Box 1028, 0315 Oslo, Norway | ³Leibniz-Gymnasium, Galileistr. 2-4, 14480 Potsdam, Germany | ⁴Evangelisches Gymnasium, Hermannswerder 18, 14473 Potsdam, Germany

Abstract The deepest geoid low globally with respect to hydrostatic equilibrium is in the Ross Sea area. Nearby in West Antarctica is a residual topography high. Both are in a region with thin lithosphere, where a mantle plume has been suggested. Hence upper mantle viscosity could be regionally reduced, allowing for faster rebound than elsewhere upon melting of the West Antarctic Ice Sheet, one of the global climate system's tipping elements. To study possible causes of the geoid low / topography high combination, we compute the effects of disk-shaped density anomalies. With -1% density anomaly and a global average radial viscosity structure, geoid low and topography high can be explained with disk radius about 10° and depth range ~150-650 km. Alternatively, there may be two separate disks somewhat laterally displaced, one just below the lithosphere and mainly causing a dynamic topography high and one below the transition zone causing the geoid low. If viscosity in the uppermost mantle is reduced by a factor 10 (from 50 to 350 km depth) to 100 (from 100 to 220 km), one shallow disk in the depth range 50-350 km would also be sufficient. In order to test the feasibility of such density models, we perform computations of a thermal plume that enters at the base of a cartesian box corresponding to a region in the upper mantle, as well as some whole-mantle thermal plume models, with ASPECT. These plume models have typically a narrow conduit and the plume tends to only become wider as it spreads beneath the lithosphere, typically shallower than ~300 km. These results are most consistent with the shallow disk model with reduced uppermost mantle viscosity, hence providing further support for such low viscosities beneath West Antarctica.

Executive Editor:
G. Peron-Pinvidic
Associate Editors:
Maëlis Arnould
Technical Editor:
Mohamed Gouiza

Reviewers:
J. Austermann
Isabelle Panet

Submitted:
23 December 2022
Accepted:
20 September 2023
Published:
21 October 2023

1 Introduction

The West Antarctic Ice Sheet (WAIS) is one of the tipping elements in the Earth's climate system (*Lenton et al.*, 2008). *Garbe et al.* (2020) show that at global warming levels of around 2 degrees above pre-industrial levels, West Antarctica is committed to long-term partial collapse leading to about 2.6 m of sea level rise owing to the marine ice-sheet instability (*Weertman*, 1974). The behavior of the ice sheet is also affected by postglacial rebound, the uplift of the lithosphere following ice sheet melting. How fast this uplift may occur depends on the viscosity of the mantle beneath the lithosphere: reduced mantle viscosity could allow for faster uplift following melting, increasing the potential stability of the WAIS against catastrophic collapse (*Barletta et al.*, 2018).

Seismic tomography (Figure 1A-C) shows low velocities beneath West Antarctica, indicative of comparatively hot temperatures and hence

low viscosities in the upper mantle and down to the upper part of the lower mantle beneath a comparatively thin lithosphere (Figure 1D). In contrast seismic velocities are fast in the upper part of the upper mantle in East Antarctica, supporting the presence of thick, cold, cratonic lithosphere. Seismic velocities are also fast in the lowermost mantle below all of Antarctica, likely caused by slabs subducted at the southern margin of the Panthalassa Ocean in the Mesozoic. Looking at various other tomography models as well as "vote maps" with Submachine (*Hosseini et al.*, 2018, <https://www.earth.ox.ac.uk/smachine/cgi/index.php>) confirms that this distribution of seismic velocities is a robust feature shared by a great number of tomography models. More details in the upper half of the mantle are seen in the regional P-wave model by *Hansen et al.* (2014): Their model shows narrower (~200-300 km wide) separate low-velocity anomalies in the upper mantle beneath Mount Erebus / Ross Sea and Marie Byrd Land, connected to a larger-scale anomaly around 660 km depth, i.e., in the lower

*✉ bstein@gfz-potsdam.de

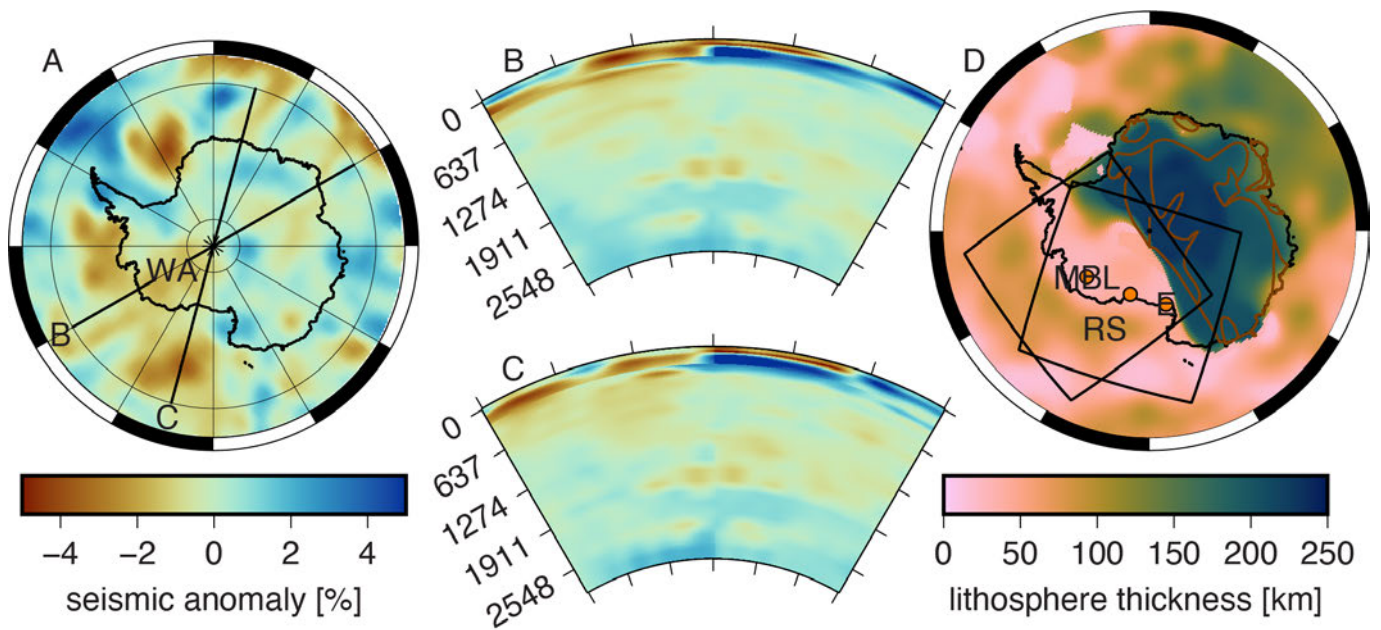


Figure 1 – **A**: Seismic velocities at depth 150 km from tomography model ANT-20 (Lloyd *et al.*, 2020). Color scales here and elsewhere in the paper from Cramer *et al.* (2018). WA = West Antarctica. **B** and **C**: cross-sections along lines marked B and C in panel A through tomography models SL2013SV (Schaeffer and Lebedev, 2013) above 200 km depth and Grand10, the 2010 model update of Grand (2002), beneath, approximately passing through the centers of the residual topography high and geoid low in Figure 3, respectively. Labels on vertical axes are depth in km (10% Earth radius spacing) **D**: Lithosphere thickness derived in Steinberger (2016) from the tomography model combination in (B) and (C). Craton outlines (Gubanov and Mooney, 2009) are drawn in brown for comparison. Squares indicate the two regional boxes for the numerical plume models, and orange dots the assumed plume locations in Marie Byrd Land, Mount Erebus and at an intermediate position. MBL = Marie Byrd Land, E = Mount Erebus, RS = Ross Sea.

transition zone and uppermost lower mantle. In contrast, the ANT-20 model of Lloyd *et al.* (2020) shows anomalies confined to the upper 200–250 km of the mantle, except in the vicinity of Marie Byrd Land where they extend into the transition zone and possibly deeper and mainly broader structures, like in the global models. Wiens *et al.* (2021) find that the slow-velocity anomalies beneath Marie Byrd Land continuing into the lower mantle in both P-wave (Hansen *et al.*, 2014) and S-wave models (Lloyd *et al.*, 2020) are consistent with a mantle plume origin for topography and volcanism. Further, transition zone thinning has been used to infer locations where plumes rise from the lower mantle: Emry *et al.* (2015) find an especially thin transition zone beneath Ruppert Coast of eastern Marie Byrd Land, around 150°W 76°S.

A mantle plume beneath West Antarctica has been first proposed by Behrendt *et al.* (1992). One surface expression could be the Mount Erebus volcano (Kyle *et al.*, 1992), but there are also numerous volcanoes in Marie Byrd Land (LeMasurier and Rex, 1989) and subglacially elsewhere in West Antarctica (van Wyk de Vries *et al.*, 2018). Presence of a plume beneath West Antarctica is also supported by high heat flux, measured directly beneath the ice sheet (Fisher *et al.*, 2015) or inferred from geophysical models (Artemieva, 2022), seismic models (An *et al.*, 2015a) or from satellite (Fox Maule *et al.*, 2005) or airborne magnetic data (Martos *et al.*, 2017). Also, the geochemical composition of volcanics in the region,

particularly in Marie Byrd Land, has been used as indication for plume origin: LeMasurier (2013) find ocean island similarities of shield volcanoes of Marie Bird Land; Panter and Martin (2022) conclude that “Marie Byrd Land magmatism results from plume material variably mixed with subduction-modified mantle; while magmatism in Victoria Land and western Ross Sea is best explained by plate dynamics and melting of asthenospheric and metasomatized lithospheric sources, and not by an upwelling plume”. However, this region overlies subducted slabs in the lowermost mantle and is far from the two Large Low Shear Velocity Provinces (LLSVPs) of the lowermost mantle and is therefore not necessarily a region where a plume from the lower mantle would be expected: Bredow *et al.* (2023) use large-scale mantle flow models to compute the conduit shape of plumes beneath West Antarctica. Their predicted source location is displaced towards the Pacific LLSVP, but still about 1500 km south of their margins. While the involvement of a plume is not clear, the existence of a rift system in West Antarctica is supported by multiple evidence (e.g., Behrendt *et al.*, 1991; Accardo *et al.*, 2014), hence there might be rift- or transtension-related decompression melting (Cooper *et al.*, 2007; Rocchi *et al.*, 2003). Moreover, the pronounced step in lithospheric thickness along the Transantarctic Mountains (Figure 1C) could lead to volcanism related to edge-driven or edge-modulated convection (Panter *et al.*, 2018). Further review of the subject of possible mantle plumes beneath

Antarctica, with appropriate references, is given by *Bredow et al. (2023)*.

Further indications on the mantle beneath are given by the geoid and dynamic topography: The geoid is usually plotted with respect to the reference ellipsoid, i.e., without the excess flattening with respect to equilibrium. Therefore, in the wider Earth science community and in the public, there is rather the prevailing impression that the deepest geoid low is just south of India. In this case, the geoid low in the Ross Sea area reaches a minimum of about -60 m (Figure 2A). However, with respect to the Earth's equilibrium shape, it exceeds -120 m (Figure 2B) and is the deepest geoid low on Earth. This has been widely recognized in the geodynamics community for a long time (e.g., *Chase and Sprowl, 1983*). When an isostatically compensated crust is corrected for, the lowest values below -125 m occur in a roughly elliptical region with half-axes ~700 km in North-South direction and 1050 km in East-West direction, approximately centered on Mount Erebus (Figure 2C). When additionally lithospheric thickness variations related to ocean floor age are taken into account, the geoid low has a localized minimum of about -130 m in the Ross Sea (Figure 3).

Residual topography (Figure 3) is derived by subtracting crustal and glacial isostatic topography and topography due to ocean floor cooling with age and is thus indicative of mantle density anomalies. High residual topography in West Antarctica, with a maximum of nearly 2 km, is thus another indication of a lower than average density and likely hotter than average mantle beneath West Antarctica. Given the spatial extent of about 2000 km for the topography high and that dynamic topography kernels above spherical harmonic degree 12 are probably rather small in the lower mantle (*Steinberger et al., 2010*), there are very likely density anomalies in the upper mantle. Comparison of residual topography and geoid shows that the maximum of residual topography is shifted by about 1600 km towards the south-southeast relative to the geoid minimum. We will discuss here the possible significance of this observation.

The right panel of Figure 3 shows characteristic profiles of the geoid across its minimum and topography across its maximum. This residual topography has been derived for a global crustal model. Uncertainties mainly depend on crustal thickness uncertainties. *Paxman (2022)* use instead the regional crustal model of *An et al. (2015b)*. They also find a regional topography high of about 2 km amplitude, but of somewhat smaller extent and with its maximum somewhat shifted and centered on Marie Byrd Land. In this case, the shift between geoid minimum (Figure 3) and residual topography maximum is reduced to about 800 km, in about the same direction.

The presence of hot low-viscosity material has also been concluded by others (*Ivins et al., 2022; van der*

Wal et al., 2022). Mostly, viscosity has been obtained by scaling seismic velocity perturbations (*Kaufmann et al., 2005; A et al., 2012*). With this approach, *Hay et al. (2017)* obtained a model characterized by a thin (~65 km) elastic lithosphere and sublithospheric viscosities reaching values as low as approximately $4 \cdot 10^{18}$ Pas beneath WAIS. Whereas *Powell et al. (2020)* even find a minimum viscosity below West Antarctica of 10^{18} Pas. The impact of 3-D viscosity structure on the the WAIS has been studied by *Powell et al. (2021)*. In a somewhat different approach, velocity anomalies translated into temperature anomalies are entered into a mantle flow law, yielding viscosities that can also depend on the stress in the mantle (*King et al., 2015*). With this approach, *van der Wal et al. (2015)* find viscosities $< 10^{19}$ Pas, and *O'Donnell et al. (2017)* viscosity $10^{18} - 10^{19}$ Pas below the West Antarctic lithosphere. Effective viscosity becomes lower for higher stress, leading to larger peaks in uplift rate (*Nield et al., 2018; Blank et al., 2021*). This also means that viscosity valid for the shorter-term glacial cycle is not necessarily the same for longer-term mantle convection. *Lau et al. (2021)* calculated a complex viscosity for Antarctic regions that accounts for this frequency dependence. *Barletta et al. (2018)* infer from uplift measured by GPS a viscosity $4 \cdot 10^{18}$ Pas beneath the marine portion of the WAIS in the Amundsen Sea Embayment, and that this shortens the GIA response time scale to decades up to a century.

Except in the context of glacial isostatic adjustment (*van der Wal et al., 2022*), there have been only a rather limited number of geodynamic models specifically about the mantle beneath (West) Antarctica. *Seroussi et al. (2017)* study the influence of a West Antarctic mantle plume on ice sheet basal conditions and find that they have an important local impact, with basal melting rates reaching several centimeters per year directly above the hotspot. *Bredow et al. (2023)* provide instantaneous geodynamic models of the excess heat flow provided by a plume. They predict a small heat flux compared to differences in surface heat flux estimates, and find that their results are not conclusive with regard to the existence of a West Antarctic mantle plume.

Dynamic mantle flow models based on mantle density models derived from seismic tomography predict high dynamic topography and a geoid low in West Antarctica (Figure 4 and *Steinberger, 2016*). Regional geoid lows with magnitude and size similar to the geoid with respect to the equilibrium shape have also been predicted based on other tomography models (*Paul and Kumar, 2022; Cui et al., 2022*). Time dependence of dynamic topography in the past 3 m.y. in the region is modelled by *Austermann et al. (2015)*. They find a significant effect on ice sheet stability.

It would of course help our understanding of the observed mantle structure, geoid and topography if we were able to reproduce it with a numerical forward model of mantle convection. However,

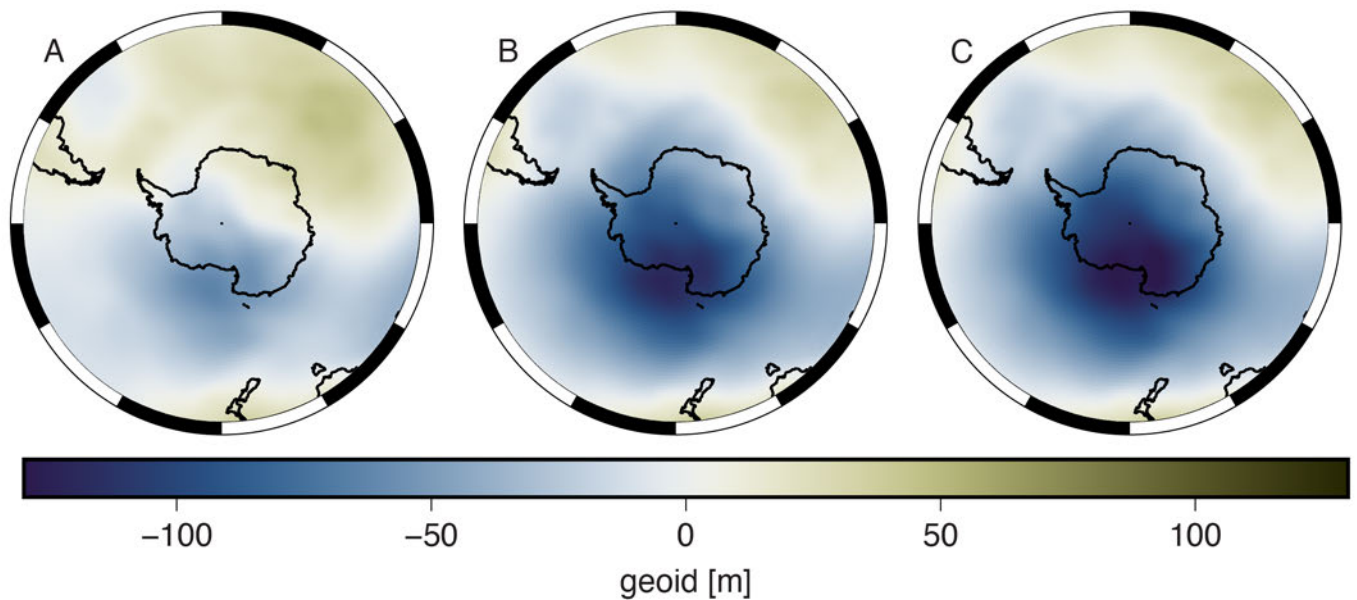


Figure 2 – Observed geoid (Pavlis et al., 2012) (A) relative to reference shape, i.e., disregarding excess flattening (B) relative to equilibrium spheroid (Chambat et al., 2010) and (C) minus contribution down to the base of the crust derived from CRUST1.0 (Laske et al., 2013) following Steinberger (2016) and assuming crustal isostasy. The geoid is expanded to spherical harmonic degree 63, with a spectral cosine taper in the degree range 32-63.

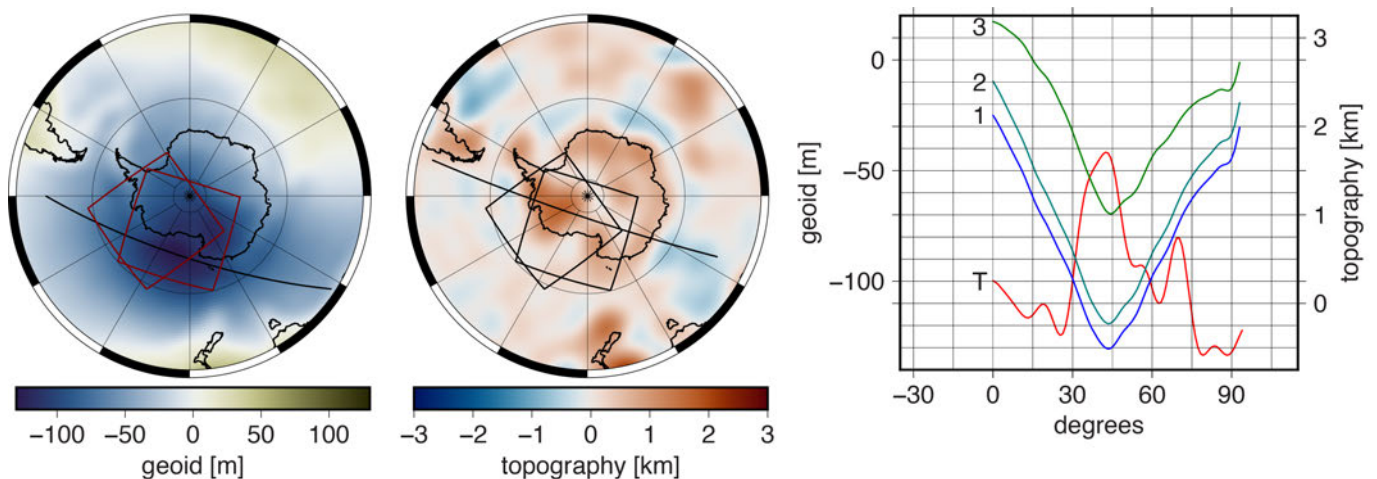


Figure 3 – Geoid as in Fig. 2 C but with also the effect of ocean floor age (Müller et al., 2008) compensated for following Steinberger (2016) and assuming isostasy, and residual topography derived in Steinberger et al. (2019). The right panel shows geoid (blue) and residual topography (red) along the profiles shown in the left and center panels. Also shown are the geoid profiles with degree-2 structure in phase with bipolarity (marked 2) and geoid after Steinberger and Torsvik (2010) (marked 3) as shown in Figure 7 removed. Squares in the left and center panels indicate regional boxes for numerical plume models.

reproducing temperatures inferred from any specific tomography model will likely not be possible, and would even not be very meaningful as long as there are strong differences among models in detail. We hence take here a simplified approach consisting of three steps:

Firstly, we show two approaches to separate upper and lower mantle contributions to the geoid. Similar to our recent paper (Steinberger et al., 2021) we argue and discuss that the geoid low in the Ross Sea area can be best explained as a superposition of a large-scale low geoid due to high-density anomalies (subducted slabs) in the lower mantle, corresponding in position to the areas of Mesozoic subduction

surrounding the Pacific (Chase and Sprowl, 1983), and a smaller-scale geoid low due to low-density anomalies in the upper mantle.

While we attempt to correct for the geoid contribution from the lower mantle, we do not make a corresponding attempt for dynamic topography. In principle there may be a large-scale dynamic topography pattern caused by the lower mantle, but the actual contribution from the lower mantle seems to be quite small (Steinberger et al., 2019). This can be reconciled with a comparatively large geoid contribution at degree two if there are no degree-two density anomalies in the 1000-2000 km depth range, which can be compatible with seismic tomography

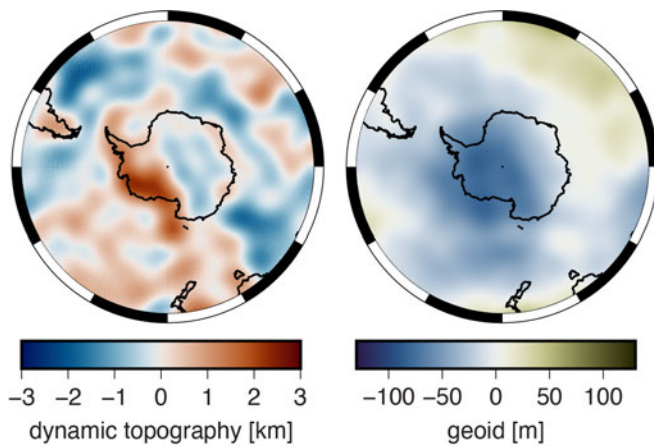


Figure 4 – Geoid and dynamic topography computed by Steinberger (2016) based on seismic tomography.

if the latter is affected by vertical smearing (Richards *et al.*, 2023).

Secondly, and similar to our approach recently taken for the Indian Ocean Geoid Low (Steinberger *et al.*, 2021) we consider synthetic disk-shaped anomalies of a given size and in a given depth range. We test for which size and depth range the predicted geoid low and dynamic topography high match observations well, and whether any synthetic models that give a good fit have a size, depth range and amplitude that is compatible with seismic tomography images.

Thirdly, we run dynamic models of mantle plumes following the approach of Gassmüller *et al.* (2016), i.e., we only model the plume in the upper mantle with a given plume location at 660 km depth. We use various modeling assumptions and parameters, and test whether we can approximately reproduce some of the simplified models of the first step which are compatible with tomography, geoid and dynamic topography. Inferring mantle temperature and viscosity from such forward plume models would then arguably be a progress compared to, or at least an alternative to, deriving it directly from seismic tomography images with their limitations in resolution, and uncertainties in conversion from seismic velocities to temperatures and viscosities. We supplement these by some models of plumes down to the core-mantle boundary at 2900 km depth, where they are generated from a thermal boundary layer.

2 Methodology

2.1 Removal of geoid contribution due to lower mantle slabs and LLSVPs

We try out two approaches in order to remove a possible degree-two lower mantle contribution related to the Large Low Shear Velocity Structures (LLSVPs) and the ring of subduction inbetween. In our first approach, we remove the degree two order two geoid contribution that is in phase with the bipolarity

in the structure of the Earth's mantle associated with the LLSVPs: For doing that, we first rotate the reference frame by an angle φ_0 such that the zero-degree longitude line approximately coincides with the LLSVPs centers, instead of Greenwich. We choose $\varphi_0 = 10^\circ$, corresponding to the geotectonic centers of Pavoni (1969, 1985), which were postulated entirely independent and much prior to the discovery of LLSVPs, but very closely correspond to LLSVP centers. The relation between the geoid coefficients in geographic coordinates (without dashes) and in the rotated reference frame (with dashes) is

$$C_{2,2} \cdot \cos 2\varphi + S_{2,2} \cdot \sin 2\varphi = C'_{2,2} \cdot \cos 2(\varphi - \varphi_0) + S'_{2,2} \cdot \sin 2(\varphi - \varphi_0) \quad (1)$$

We use the addition formulas for sines and cosines and thus obtain two separate equations for terms with factor $\sin 2\varphi$ and with factor $\cos 2\varphi$, respectively. We can solve these equations to compute $C'_{2,2}$ and $S'_{2,2}$ in terms of $C_{2,2}$, $S_{2,2}$ and φ_0 . We then conversely express $C_{2,2}$ and $S_{2,2}$ in terms of $C'_{2,2}$, $S'_{2,2}$ and φ_0 , and obtain the in-phase contribution (line 7 marked LLSVPs in Table 1) by setting $S'_{2,2}$ to zero, and the geoid with that contribution removed (line 8 marked LLSVP-corr in Table 1) by setting $C'_{2,2}$ to zero. Spherical harmonics degree two order two of the in-phase contribution has maximum and minimum of $\pm C'_{2,2} \cdot \sqrt{15}$ at the equator and is zero at the pole, whereas degree two order zero is $C_{2,0} \cdot \sqrt{5}$ at the pole and $-C_{2,0} \cdot \sqrt{5}/2$ all along the equator. Requiring that the combination for the total bipolarity structure has the same value at the pole as the minimum at the equator we obtain $C_{2,0} = -C'_{2,2}/\sqrt{3}$ (line 7 in Table 1).

However, there may be additional geoid lows close to the poles because the plate configuration in the Pacific / Panthalassa has changed such that there was more subduction towards north and south at earlier times and more towards east and west of Pacific / Panthalassa at more recent times. This means that slabs north and south of the Pacific tend to be deeper, hence contribute a geoid low in contrast to a geoid high east and west. This is treated in Steinberger and Torsvik (2010) and we hence, in our second approach subtract the geoid due to LLSVPs and subducted slabs (which, beneath Antarctica, are mostly in the lower mantle) from their work. They use plate reconstructions and geodynamic forward modelling to infer slab distribution through time, and assume that the LLSVP contribution has remained constant. The geoid due to LLSVPs is adjusted such that the fit of the total geoid to the observed geoid is optimized. They use the same spherical harmonic method as here to infer the geoid from the (slab and LLSVP) density distribution.

Table 1 – Geoid potential coefficients with modifications in units of 10^{-6} . total: As listed by Pavlis et al. (2012). ellipsoid: Ellipsoidal reference shape. Further even-degree order-zero coefficients are also non-zero but small and negligible. reference: Coefficients relative to reference shape. equilibrium: Coefficients relative to equilibrium shape from Chambat et al. (2010). crust-corr: Crust corrected as in Figure 2. All other coefficients are also slightly changed. age-corr: Also corrected for seafloor age as in Figure 3. Again, other coefficients also slightly changed. LLSVPs: Degree-two in phase with bipolarity structure (Pavoni, 1985) as in Figure 7A. LLSVP-corr: Coefficients corrected for the crust, for seafloor age and for LLSVPs as given by the line just above, as in Figure 7B. Note that the computation and subtraction for Figure 7C and D are done on a grid, hence no coefficients are listed here.

	$C_{2,0}$	$C_{4,0}$	$C_{2,2}$	$S_{2,2}$
total	-484.165	0.540	2.439	-1.400
ellipsoid	-484.165	0.790	0	0
reference	0	-0.250	2.439	-1.400
equilibrium	-5.10	-0.446	2.439	-1.400
crust-corr	-5.19	-0.463	2.568	-1.361
age-corr	-5.01	-0.292	2.661	-1.585
LLSVPs	-1.130	0	1.840	0.670
LLSVP-corr	-3.883	-0.292	0.821	-2.255

2.2 Computations with spherical harmonic code

Geoid and dynamic topography can be computed from a spherical harmonic expansion of mantle densities and flow for a viscous rheology with only radial viscosity variations (Hager and O’Connell, 1979, 1981). We use this approach for density anomalies that we refer to as shaped like a cylindrical disk, although this is not strictly the case, because of Earth’s curvature. Also, we typically consider lateral smoothing, i.e., there is no sharp density contrast at the edge of the cylinder, but a smooth transition from zero to total anomaly, following a cosine function over a distance specified in degrees of arc measured from the center of the cylinder. Geoid and dynamic topography are computed first individually for each spherical harmonic degree, by multiplying, at each depth, density with a depth-dependent kernel for the geoid (Richards and Hager, 1984; Ricard et al., 1984) or topography, and integrating over depth, before adding up the contributions of different spherical harmonics. We adopt the viscosity structure from Steinberger (2016) with a free-slip surface, as we have shown there that it is suitable to model geoid and dynamic topography globally. Dynamic topography kernels are always negative, i.e., a negative density anomaly always leads to uplift, but the geoid kernels include the positive contributions of internal density anomalies and negative contributions of dynamic surface and core-mantle boundary topography. Either contribution can be dominant, so kernels may be either positive or negative and the shape of the kernels as a function of depth can be quite variable for different spherical harmonic degrees (See Fig. 2 of Steinberger et al., 2021). Given that

different spherical harmonic degrees contribute to the disk-shaped anomalies, the results are not straightforward. We also consider “410” and “660” phase boundary topographies due to Clapeyron slope, adopting parameters from Steinberger (2007). Our density model consists of 50 km thick layers where the effect of extra or missing masses is computed as if they would all occur in the middle of each layer, e.g., for a disk between 150 and 650 km at 175 km, 225 km, ..., 625 km. The effect of phase boundaries is always assigned to the layer above them, i.e., the “410” at 375 km and “660” at 625 km, such that, for example, the effect of the “660” is already included in the disk between 150 and 650 km. Considering phase boundaries with parameters from Steinberger (2007) amounts to multiplying the density anomaly at 375 km with a factor 3.56 (i.e., replacing a -1% density anomaly by -3.56%) and the one at 625 km with a factor -0.78 (i.e., replacing a -1% anomaly by +0.78%). Whether or not the effect of a phase boundary is included makes a substantial difference, however, we find that it makes hardly any difference whether the effect is included in the layer above or below the phase boundary. For a thermal expansivity of $2 - 3 \cdot 10^{-5}/K$, a -1% density anomaly corresponds to 333-500 K which is rather on the high end of what is realistic. However, results can be simply scaled down linearly to lower temperatures.

The neglect of lateral viscosity variations (LVV) will lead to an over-estimate of dynamic topography in regions of low viscosity. Since dynamic topography gives a positive geoid contribution, this means that with LVV, a geoid low above a low-viscosity and low-density cylinder will be somewhat more pronounced than without LVV. In order to be able to estimate this difference, we approximately estimate the geoid height N corresponding to only the dynamic topography contribution H : From the Bouguer formula, the corresponding gravity anomaly is

$$\delta g = 2\pi\rho_0GH \tag{2}$$

where ρ_0 is the appropriate density for dynamic topography (uppermost mantle; $3.3 \cdot 10^3 \text{kg/m}^3$), and G is the gravity constant. From the solution for Laplace’s equation $\nabla^2 V = 0$ for the gravity potential V , with a wavelength λ in both x and y direction:

$$V = \sin \frac{x \cdot 2\pi}{\lambda} \cdot \sin \frac{y \cdot 2\pi}{\lambda} \cdot \exp - \frac{z \cdot \sqrt{2} \cdot 2\pi}{\lambda}$$

we obtain a gravity anomaly equal to its vertical derivative:

$$\delta g = \frac{\partial V}{\partial z} = - \frac{\sqrt{2} \cdot \pi}{\lambda} V \tag{3}$$

Setting eqs. 2 and 3 equal yields $V = -\rho_0GH\lambda\sqrt{2}/2$, and hence a geoid height $N = -V/g_0$ where $g_0 =$

$4\pi G\rho_{00}r_E/3$ is normal gravity at the Earth surface, $\rho_{00} = 5.5 \cdot 10^3 \text{ kg/m}^3$ is the average density of the Earth, and r_E is the Earth radius. Combining these equations yields a ratio of geoid to dynamic topography amplitude $N/H = 3\sqrt{2}/(8\pi) \cdot (\rho_0/\rho_{00}) \cdot (\lambda/r_E)$. With $\lambda = 3126 \text{ km}$ that is about 5 %. We will use this estimate in the discussion section.

2.3 Computations with ASPECT

The work flow for the models with ASPECT (Advanced Solver for Problems in Earth's ConvecTion) (Kronbichler et al., 2012; Heister et al., 2017) was initially developed by Gassmüller et al. (2016). This extended version of ASPECT (available at this GitHub repository) was used in Model runs 1-3. For all other models, we upgraded to ASPECT main branch version 2.4.0-pre (Bangerth et al., 2021a,b). In this case, all boundary temperatures, initial temperatures and boundary velocities were explicitly prescribed through Ascii data files. The description of how initial and boundary temperature was inferred from lithosphere thickness only refers to this version.

Our thermal plume model computations were performed in a 3-D cartesian box extending 3300 km x 3300 km horizontally and 660 km vertically. One drawback of using a box model is that the geoid cannot directly be computed in ASPECT, as the geoid postprocessor can only be used if the geometry is a sphere, spherical shell or spherical chunk. To convert from spherical coordinates, in which global mantle flow, lithosphere thickness and plume positions are given, to cartesian coordinates, a Lambert equal area projection was used. Models 1-3 use a projection center at 126°W, 77°S, centrally located in West Antarctica. For the remaining models, the projection center was shifted westward to 163°W, 79°S such that a possible plume located beneath Mount Erebus at 167.2°E, 77.5°S is not too close to the boundary of the model box

Lithosphere thickness is adopted from Steinberger (2016) (Figure 1C). Initial and boundary temperatures $T(x, y, z)$ are computed from lithosphere thickness $t_{lith}(x, y)$

$$T = T_{ad}(z) - 1340 \text{ K} \cdot \text{erfc}(z/t_{lith}(x, y))$$

where x and y are horizontal coordinates, z is depth and erfc stands for the complementary error function. Otherwise the temperature structure develops self-consistently. The adiabatic temperature profile $T_{ad}(z)$ and two temperature profiles, approximately representing West and East Antarctica, are shown in Figure 5 (left graph).

Viscosity is depth- and temperature dependent:

$$\eta(z, T) = \eta_r(z) \exp\left(-\frac{rH(z)(T - T_{ad}(z))}{RTT_{ad}(z)}\right) \quad (4)$$

We use several different radial profiles (corresponding to adiabatic temperature) $\eta_r(z)$

shown in Figure 5 which correspond to different asthenosphere thicknesses (or no asthenosphere at all). The red profile approximately corresponds to Steinberger et al. (2010). A linear viscosity variation is assumed between lower mantle and the lower part of the upper mantle, and between the lower part of the upper mantle and asthenosphere. Since we plot viscosity on a logarithmic scale, this linear variation appears curved. Since these radial viscosity profiles correspond to adiabatic temperature, they do not increase towards the surface, but obviously, there will be a viscosity increase towards the surface anywhere in our model, due to the (non-adiabatic) temperature decrease in the lithosphere towards the surface.

Viscosity variations due to non-adiabatic temperatures depend on rH/R where H is activation enthalpy, $R = 8.3144 \text{ J/K/mol}$ is the universal gas constant and appropriate values for the factor r are 1 for diffusion creep but less than 1 for dislocation creep or a combination of both creep mechanisms (Christensen, 1983). The blue line in Figure 5 corresponds to $r = 1/3.5$, the green line to a larger r (but still less than 1). For the lower mantle (not shown) we use $r = 1$ and H increases from $3.4 \cdot 10^5 \text{ J/mol}$ at its top to $5.2 \cdot 10^5 \text{ J/mol}$ at the CMB. Cutoff viscosities are 10^{19} Pas as lower bound and 10^{23} Pas as upper bound.

Plume influx and temperature anomaly are prescribed at the bottom. The plume conduit has a radius of $r_c = 130 \text{ km}$ with $T_c = 200 \text{ K}$ temperature anomaly and an inflow velocity $v_c = 5 \text{ cm/yr}$. We apply Gaussian profiles, i.e. we add a temperature $T_c \cdot \exp(-(r/r_c)^2)$ and apply a vertical inward velocity $v_c \cdot \exp(-(r/r_c)^2)$ at a distance r from the plume center. For the initial temperature, we add 300 K within 250 km distance from the plume center at the lowermost layer (depth 650 km) and 82 K in the second layer. In cases 1-3, an initial plume head with radius $r_h = 250 \text{ km}$ with $T_h = 300 \text{ K}$ temperature anomaly and inflow velocity $v_h = 8 \text{ cm/yr}$ is also implemented.

This time was chosen because the plume takes approximately 4 Myr to reach the surface, so it would correspond to an initiation of volcanism at around 30 Ma (Hole and LeMasurier, 1994). It also corresponds to the onset of glaciation in Antarctica (Lear et al., 2000) which may be coincidental, but there may also be a causal relation, as the dynamic topography increase caused by the rise of a plume head or pulse towards near the surface may be conducive to the onset of glaciations, as has been proposed for Greenland (Steinberger et al., 2015). However, the primary drivers for rapid Cenozoic glaciation of Antarctica are believed to be the tectonic opening of Southern Ocean gateways, which enabled the formation of the Antarctic Circumpolar Current and the subsequent thermal isolation of the Antarctic continent (Kennett, 1977) and/or declining atmospheric CO_2 (DeConto and Pollard, 2003).

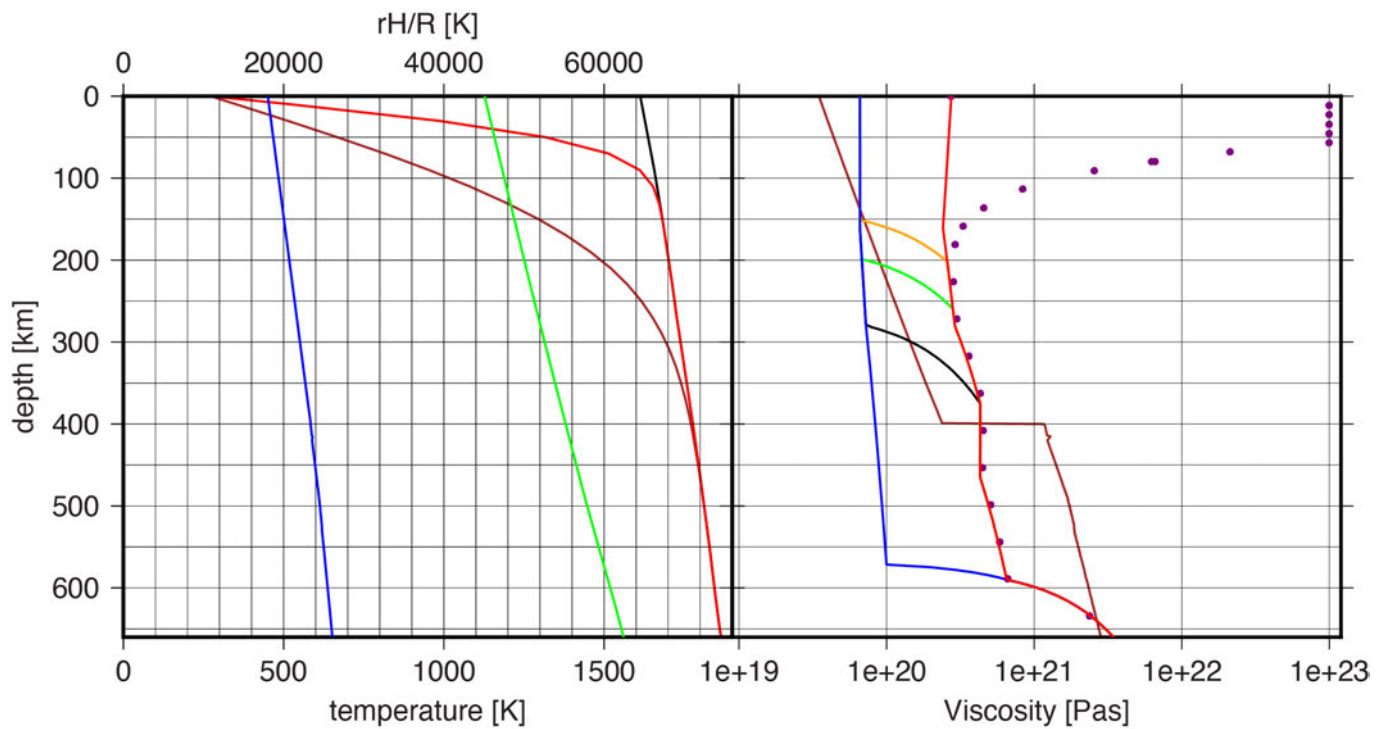


Figure 5 – Left panel, lower x-axis: Adiabatic temperature profile (black) and two radial temperature profiles for lithosphere thickness of 60 km (red) and 200 km (brown). **Left panel, upper x-axis:** Profiles of rH/R characterizing temperature dependence of viscosity (equation 4). **Right panel:** Different (adiabatic) radial viscosity profiles $\eta_r(z)$. For five of the profiles (black, orange, red, green, blue) results are shown. The brown profile corresponds to the viscosity structure used for the global flow model, but with continuous viscosity variations in upper mantle and transition zone. Results for this case are not shown, as they remain very similar to those already shown. Purple dots show viscosities corresponding to the red profile and a 100 km thick lithosphere; upper viscosity cutoff 10^{23} Pas.

In the uppermost ~200 km of the side boundaries and at the surface, velocities are set to zero, corresponding to zero plate motions. Given that Antarctica has hardly moved over the mantle since 34 Ma (Dobrovine et al., 2012), and that the Antarctic plate covers most of the model box (any plate boundaries would be at most close to the edges) this setting appears appropriate, and it is not expected that using more realistic boundary conditions above 200 km depth would greatly affect results. Because plate motions are not considered here, and lithosphere thickness doesn't change that much over 34 Myrs, it appears appropriate to use the model of present-day thickness for the model initiation.

Elsewhere velocities on boundaries are either prescribed based on a global mantle flow model computed with a spherical-harmonic based approach as e.g., described in Gassmüller et al. (2016), or set to zero. Global mantle flow is computed with the more recent viscosity structure SL+Gra3 from Steinberger (2016). Although we vary the regional viscosity model, we prefer to keep the same viscosity structure for global flow, in order to be able to better distinguish the effects of global flow boundary condition and regional viscosity structure. We also used the viscosity structure corresponding to global flow (brown profile in Figure 5) for the regional model. However, results for this case are not shown, as they remain very similar to results shown.

In the first case (GF=C) we use the same surface plate velocities as in Gassmüller et al. (2016) and the present-day density model that includes thermochemical piles in the lowermost mantle from Steinberger (2016). This model is only used for present-day flow. In the second case (GF=TD) the density model is derived from the tomography model TX2019slab (Lu et al., 2019) in a spherical harmonic expansion up to degree and order 63 on 58 radial layers from depth 2875 km to 25 km at distance 50 km, provided by Thorsten Becker. We use here a simple conversion $(\delta\rho/\rho)/(\delta v_s/v_s) = 0.25$ from relative seismic velocity to relative density variations below depth 200 km and disregard anomalies above 200 km. There, thermal diffusion plays an important role and hence backward advection, which we use to compute past density and flow, is less appropriate. Also, such a simple thermal conversion is less appropriate in the lithosphere, where compositional variations may affect both density and seismic velocity. This means we also disregard thermochemical piles as they won't influence the upper mantle flow field by much. In this case, the velocity boundary condition is time-dependent due to advection of density anomalies and time-dependent plate motion boundary conditions for global flow computation.

The total influx and outflux of the model box are not exactly balanced because (i) boundary velocities in the uppermost 200 km are set to zero (ii) the

Table 2 – Model parameters: Center of model box, position of plume inflow at the bottom of the box, Lith: Lithosphere thickness - C = constant 100 km, V = variable as inferred from tomography model GF: Global flow (N=no, C=time-independent flow; density model as Steinberger (2016), TD=time-dependent flow; density model inferred from TX2019slab (Lu et al., 2019). In the latter two cases cutoff at constant depth 200 km. η_{ad} : radial viscosity model corresponding to adiabatic temperature. Colors given correspond to Fig. 5 right. η_{mad} : Model for viscosity variations due to deviations from adiabatic temperature. hi = strong dependence, corresponding to green line in Fig. 5 left. lo = weak dependence, corresponding to blue line. The asterisk at Models 1-3 indicates that these models were computed with the ASPECT “Reunion branch”. Bold entries are the “reference setting”, thus case 9 is the reference case. For each case, another case can be found that only differs in 1 column, such that the effect of changing that particular model setting can be extracted.

#	Center	Plume	Lith	GF	η_{ad}	η_{mad}
1*	126°W, 77°S	126°W, 77°S	C	N	black	hi
2*	126°W, 77°S	126°W, 77°S	V	N	black	hi
3*	126°W, 77°S	126°W, 77°S	V	C	black	hi
4	163°W, 79°S	167.2°E, 77.5°S	V	C	orange	lo
5	163°W, 79°S	167.2°E, 77.5°S	V	C	red	lo
6	163°W, 79°S	163°W, 79°S	V	C	red	lo
7	163°W, 79°S	163°W, 79°S	V	TD	green	lo
8	163°W, 79°S	163°W, 79°S	V	TD	blue	hi
9	163°W, 79°S	163°W, 79°S	V	C	black	lo
10	163°W, 79°S	163°W, 79°S	V	C	black	hi
11	163°W, 79°S	163°W, 79°S	V	TD	black	hi
12	163°W, 79°S	163°W, 79°S	V	TD	black	lo

conversion from spherical to cartesian boxes implies a distortion (iii) the plume influx is prescribed. We therefore compute the integrated flux over all boundaries of the box (bottom and four sides) and add a velocity orthogonal to the boundary at all four side boundaries below 200 km depth (not at the bottom) such that the total influx/outflux adds up exactly to zero. The resulting present-day boundary velocities in the second case are shown in Figure 6.

We use constant gravity 9.81 m/s². The heating model includes adiabatic heating, latent heat and shear heating. Other material properties are adopted from the “Steinberger” model provided with ASPECT. We conducted altogether 12 upper mantle model runs with varying parameters and assumptions as listed in Table 2.

In order to ascertain that results do not critically depend on just modeling the upper mantle, we also ran models without global flow but with free-slip side boundaries that extend down to the core-mantle boundary at 2900 km depth. We use 4000 K, 3500 K, 3250 K and 3000 K for CMB temperatures T_{CMB} . The higher values are closer to recent independent CMB temperature estimates (Lobanov et al., 2021) but the lower values yield more appropriate plume temperatures close to the surface (Herzberg and Gazel, 2009; Bao et al., 2022), and might e.g., mimic plumes rising from the tops of thermochemical

piles (especially near their margins). We model the thermal boundary layer at the base of the mantle at the initial time by adding $(T_{CMB} - T_{ad,CMB}) \cdot \text{erfc}(h/100\text{km})$ where h is height above the CMB. We “seed” the plume by adding a temperature $T_{seed} \cdot \exp(-(d/d_0)^2) \cdot h/h_0 \exp(-h/h_0)$ where d is the horizontal distance from the center of the box. We use $d_0=100$ km, $h_0=100$ km and $T_{seed}=500$ K, except for the case with $T_{CMB}=3000$ K, where all these values are doubled, such that the plume develops faster, before the lithosphere grows unreasonably thick.

Radial viscosity in these whole mantle models corresponds to the red curve in Figure 5, i.e., also follows Steinberger et al. (2010) in the lower mantle (not shown), but with constant viscosities at the base of the mantle, as the viscosity drop there comes in due to non-adiabatic temperature increase (like for the lithosphere).

3 Results

3.1 Residual geoid due to upper-mantle low-density anomalies

The lower-mantle degree-two contribution determined with the first approach in section 2.1 is shown in Figure 7A, the geoid with this contribution removed in Figure 7B. Comparing profiles in Figure 3 shows that this reduces the amplitude of the geoid minimum by about 12 m, while the shape of the anomaly remains very similar.

The lower-mantle contribution determined with the second approach is shown in Figure 7C. In this case, the shape of the remaining anomaly is again similar while its amplitude is reduced from about 130 m to 70 m: This occurs, because the lower mantle “slab vs. LLSVP” structure give a very broad low of about 60 m amplitude, on top of which a smaller-scale geoid low of about 70 m amplitude is superimposed. The remaining low (Figure 7D) has an extent of ≈ 7000 km corresponding to spherical harmonics $l \geq 6$ for which geoid kernels are likely comparatively small in the lower half of the mantle. Hence we regard 70 m the most realistic estimate for the contribution from a low-density anomaly in the upper mantle and perhaps upper part of the lower mantle to which modeling results should be compared.

3.2 Synthetic model results obtained with spherical harmonic code

We now show results of our simple models for synthetic disk-shaped anomalies of a given size and depth range. Figure 8 shows results for our reference case, with smoothing from 5 to 15 degrees, and additionally some profiles with different smoothing. Smoothing in radial direction somewhat changes the amplitudes, because of the radial sensitivity of geoid and topography. Hence, for a simpler interpretation of results, we do not apply radial smoothing in the

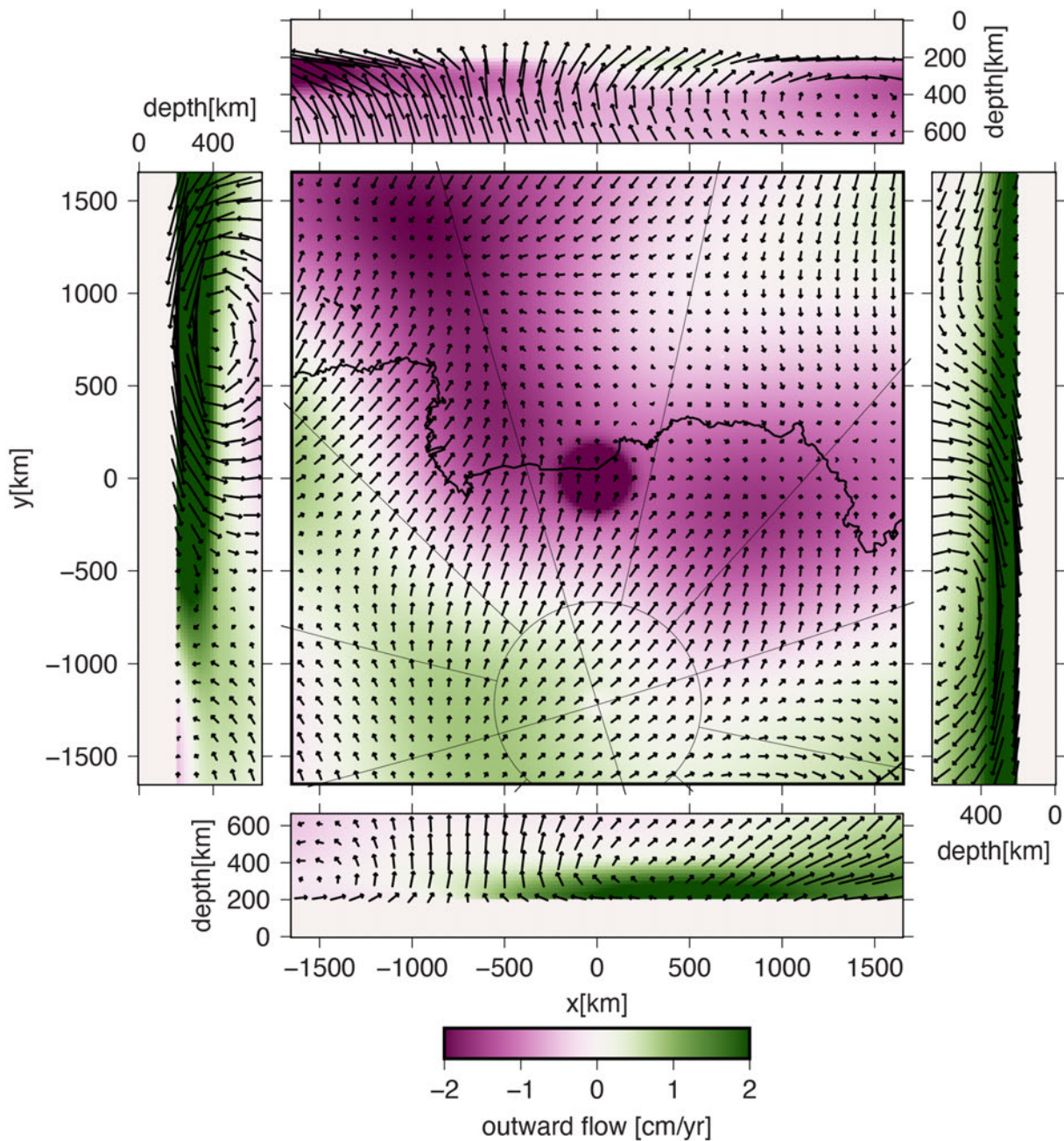


Figure 6 – Velocity boundary conditions, derived from global flow model “TD” for present-day and plume influx. Center of the model box at 163°W, 79°S. Flow component parallel to boundaries represented by arrows, with length proportional to speed; 100 km corresponds to 1 cm/yr.

following. In comparison with Fig. 3, the size of the dynamic topography anomaly is about the same, but its amplitude is somewhat larger (~3 km vs. 2 km). For the geoid, the predicted amplitude (~80 m) is somewhat less than observed (~130 m) but if the contribution from lower mantle slabs and LLSVPs is removed (Figure 7D; here blue-green dotted line) the amplitude is very similar – about 70 m. The possible effect of lateral viscosity variations on the respective amplitudes will be discussed in the next section. 20 degrees of arc lateral extent of the anomaly in the reference case is also similar to what tomography shows. Figure 1 shows one representative case; a large number of tomography models can be visualized with Submachine (*Hosseini et al., 2018*, <https://www.earth.ox.ac.uk/smachine/cgi/index.php>).

Anomalies in tomography models tend to extend even deeper, down to ~1000 km. However, the -1% amplitude of the synthetic density anomaly would correspond to about -4% S-wave anomaly, which tomography models reach at most in the upper ~200 km.

Figure 9 shows how amplitude and shape of geoid and dynamic topography anomaly depend on radius of the cylindrical disk, as well as its top and bottom depth. The radius of the disk does not only affect the lateral extent of the anomaly but also its amplitude. This is especially the case for the geoid: Only for the largest disk radius, the geoid can reach an amplitude of the order 100 m as observed. An amplitude of about 70 m, which is estimated after removing

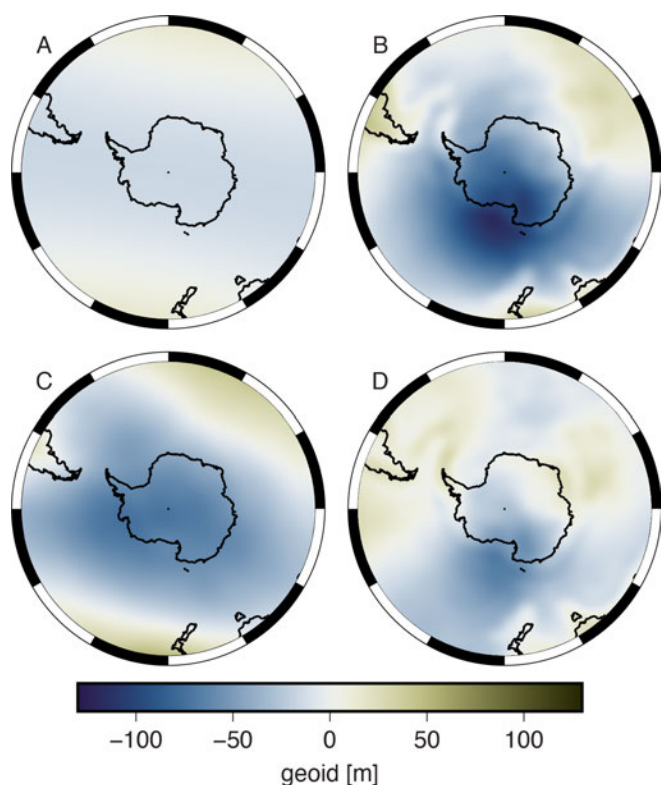


Figure 7 – (A): Geoid degree-2 structure in phase with the bipolarity (Pavoni, 1985) associated with LLSVPs. (B): Geoid contribution in (A) removed from the one shown in Figure 3. (C): Geoid related to LLSVPs and slabs after Steinberger and Torsvik (2010) (D): Geoid contribution in (C) removed from the one shown in Figure 3.

the contribution from slabs and LLSVPs, can still be achieved for a 7.5 degree disk if the bottom of the disk is 750 km deep, or even deeper. Of course, a higher amplitude could also be achieved with a stronger anomaly, but 1% is already quite strong, corresponding to a temperature anomaly of the order 400 K. Also, the bottom of the disk needs to be at least in the transition zone at ~550 km or deeper, in order to yield a sufficient geoid anomaly. In contrast, predicted dynamic topography anomalies tend to be rather too large: If the bottom of the disk is at 550 km or deeper, its top needs to be at least 150 km deep such that predicted dynamic topography is not too large. There is very little difference between results with the bottom of the disk at 550 km and 650 km, as the effect of phase boundary deflection nearly compensates the buoyancy in the 550 to 650 km layer. A deeper bottom of the disk (e.g., shown for 750 km vs. 650 km) gives a more pronounced geoid low, whereas the fractional change of dynamic topography is less. Hence, by making the disk extend even deeper, it will be possible to reduce the amplitude of the density anomaly and still maintain a good fit to geoid and dynamic topography, and even improve the geoid-to-topography ratio. This is somewhat at odds with tomography showing the strongest anomalies just below the lithosphere, similar also to the dynamic models shown next. Below, we will however show that this discrepancy

can become less if viscosity is reduced in a layer below the lithosphere. Similarly, in the next section, we will qualitatively show that consideration of lateral viscosity variations may somewhat reduce predicted dynamic topography and increase predicted geoid.

Hansen et al. (2014) suggest a mantle plume ponded below the 660 km discontinuity beneath MBL to explain what they see in tomography. This points to the possibility that the dynamic topography high and geoid low are due to separate “disks” associated with the same upwelling (plume): The dynamic topography high mostly due to the plumehead spreading beneath the lithosphere and the geoid low due to low-density material just below the transition zone. The displacement of the dynamic topography maximum relative to the geoid minimum could then be due to a lateral displacement of the disk centers relative to each other, rather than tilt of the plume. An example for a result with two separate disks is shown in Figure 10. Anomaly sizes vary with disk sizes, hence those were chosen such that dynamic topography and geoid approximately match with observations (after removing the lower mantle contribution for the geoid). An upper disk with 7.5 degrees radius also approximately matches the time-dependent dynamic models in the next section. However, low-density material in or below the transition zone could only cause a geoid low if its buoyancy is larger than the compensating effect of an upward-deflected 660 km discontinuity, which raises the question why it would be “ponded” at that depth and not rise straight to the surface.

Results so far were all computed for the same viscosity structure designed to fit geoid and dynamic topography globally (Steinberger, 2016). However, due to the presence of a plume, viscosity may be locally reduced in parts of the upper mantle. To accommodate that, we try cases with a 10- or 100-fold reduced viscosity either in the 100-220 km “asthenosphere” depth range or in the entire depth range of the cylindrical disk. Such a reduced viscosity will lead to reduced dynamic topography and hence increased geoid low, hence we expect an improved fit even for a disk reaching the base of the lithosphere assumed at depth 50 km. Results in Figure 11 show that this is indeed the case: Especially for a disk in the depth range 50-350 km we can get a rather good fit to both geoid and dynamic topography, either for a viscosity reduced by a factor 10 in the same depth range of the disk and 50 km thick lithosphere (green dashed line) or by a factor 100 in the 100-220 km range. We will get back to this result in the discussion and explain why we consider these our most realistic results and what might be the cause. Results are shown for 8 degrees of arc disk radius, but remain similar, with somewhat increased size and amplitude for 10 degrees. For 3 or 5 degrees disk radius, the lateral extent of predicted anomalies is somewhat too small. Again, 8 degree disk radius also approximately matches the dynamic forward models in the next section.

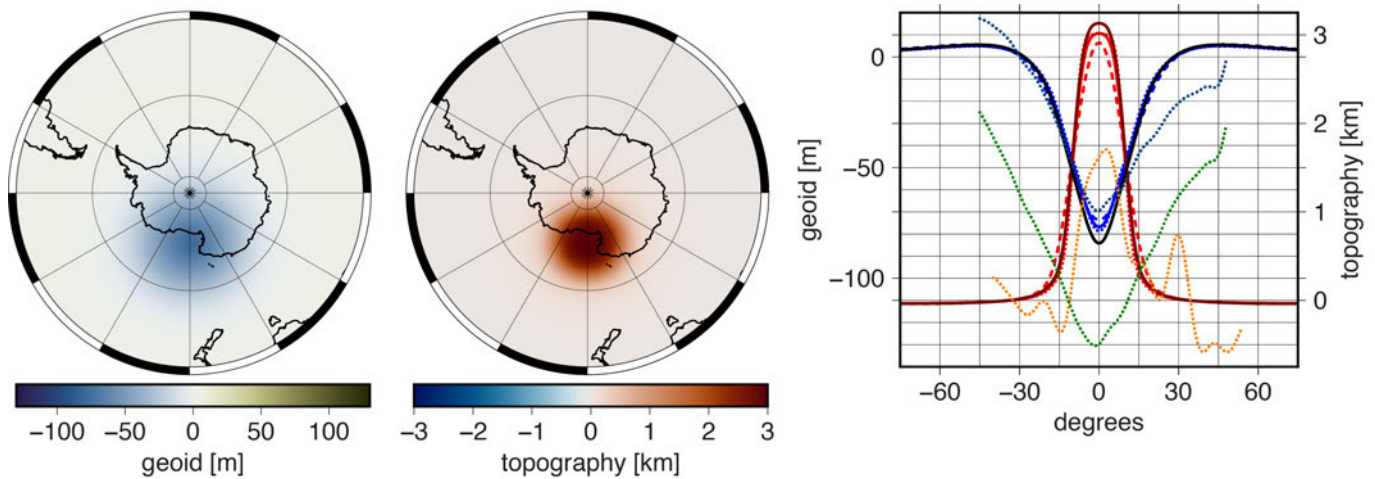


Figure 8 – **Left:** Geoid for reference case (disk of -1% density anomaly in depth range 150 km to 650 km; 10 degrees of arc radius with cosbell smoothing from 5 to 15 degrees; center of disk at 75° S, 180° longitude). **Center:** Dynamic topography for reference case. **Right:** Profiles of geoid (blue) and dynamic topography (red) across center of disk. In addition to reference case (solid blue and red lines) we also consider cases with smoothing from 0 to 20 degrees (dashed), and without smoothing (dotted). Dark red and black lines like red and blue, except that here the anomaly is also smoothed in radial direction with cosine tapers from 0 to 300 and 400 to 700 km. Observation-based profiles as in Figure 3 are shown as green (geoid), blue-green (geoid with slab and LLSVP contribution removed) and orange (residual topography) dotted lines.

3.3 ASPECT results

Results are shown in Fig. 12 and 13. Despite various differences, the results are all similar in that there tends to be a narrow conduit of the order 200 km width or less - much less than the disk-shaped anomaly considered above, and the plume only spreads to a larger lateral extent at above 200 km in most cases, reaching about 300 km if it spreads below thick lithosphere. This is shallow compared to the depth range suitable to explain the geoid. Without global flow (cases 1 and 2), the plume rises vertical and spreads laterally in all directions. But with global flow, the plume conduit gets tilted in the “mantle wind” and below the lithosphere plume material tends to flow in the same direction in which the conduit is tilted. But this direction depends on the position of the plume: If the plume is centrally located in West Antarctica (case 3) it is eastward, if it is located further west, beneath Mount Erebus (cases 4 and 5), it is westward, such that plume material is actually being pushed beneath the thicker lithosphere of East Antarctica. If it is in an intermediate location (cases 6-12) towards WSW (for flow model “C”, cases 6,9,10) to SSW (for flow model “TD”, cases 7,8,11,12). These deflection directions correspond to the flow at the boundaries of the model box: While the upper 200 km are kept at rest (corresponding to zero plate motion), flow is mostly outward immediately below on the left (ca. west), right (ca. east) and front side, and inward on the back side (Figure 6). In the cases with flow model “TD”, plume tilt and asymmetry is considerably stronger as with model “C” (especially compare cases 11 and 10, which are otherwise identical). Thickness of the plume conduit depends on both radial viscosity structure and lateral viscosity variations: Case 8 with the lowest overall viscosity and strong lateral viscosity variations yields

a very thin conduit, compared to other cases. In comparison, the conduit is thicker in case 11, where the viscosity is higher in the lower part of the upper mantle and even thicker in case 12 with low lateral viscosity variations. The fattest conduit results for the highest viscosity (cases 5 and 6), but it is still only about 200 km wide.

On top of the temperature cross-sections, we also plot dynamic topography profiles. Lithospheric thickness variations are also associated with a strong dynamic topography signal in this model, but by visually matching with the temperature cross-section, we can estimate that the dynamic topography signal associated with the plume is about 1-2 km, very similar to the observation-based residual topography. It is not possible to directly compute the geoid with ASPECT in cartesian box geometry, however, below we will at least use ASPECT results to estimate the effect of lateral viscosity variations on the geoid.

Results for whole-mantle models are shown in Figure 14 again 30 Myrs after the plume head reaches the lithosphere. Because plumes tend to take a long time to develop in these models, the lithosphere has become thicker by then. But apart from that, results are similar in that plumes tend to spread as a ~100 km thick “pancake” below the lithosphere. We use here different color scales for different CMB temperatures. Only in the case of the lowest CMB temperature 3000 K (~465 K temperature contrast across bottom TBL) the maximum plume temperature anomaly is around 200-250 K, which is similar to the other cases. For a higher, more realistic CMB temperature, the plume maximum temperature also becomes much higher. This discrepancy may indicate that plumes do not rise directly from the CMB but perhaps from the tops of thermochemical piles. However, this

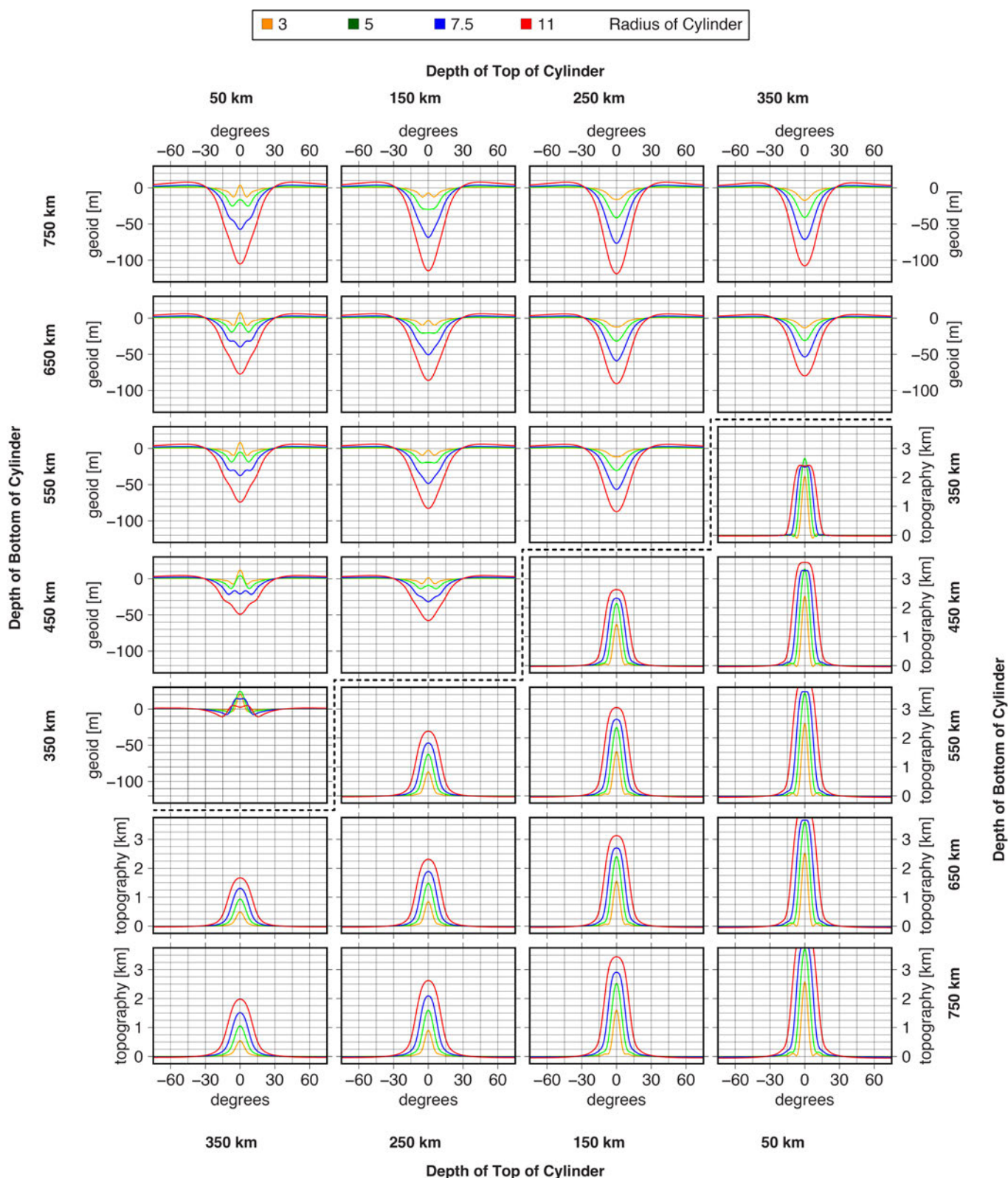


Figure 9 – Dependence of geoid (top left panels) and dynamic topography (bottom right panels) on the radius and depth range of a low-density cylindrical disk in the upper mantle, along profiles across the center of the anomaly. Radius is given by color (see legend), top and bottom of disk are indicated on the edges of the figure. Radial smoothing from 0.5 to 1.5 times disk radius.

will not be further discussed here. The case with CMB temperature 4000 K (not shown) yields an even higher plume temperature, as well as more small-scale structure in the plume head, presumably due to lower viscosity.

One simplification that we have done in our geoid and topography computations was the neglect of lateral viscosity variations. However, we estimate their effect by comparing two ASPECT box models for the whole mantle with lateral extent of 9900 x 9900 km, and a cylindrical anomaly as in the reference case

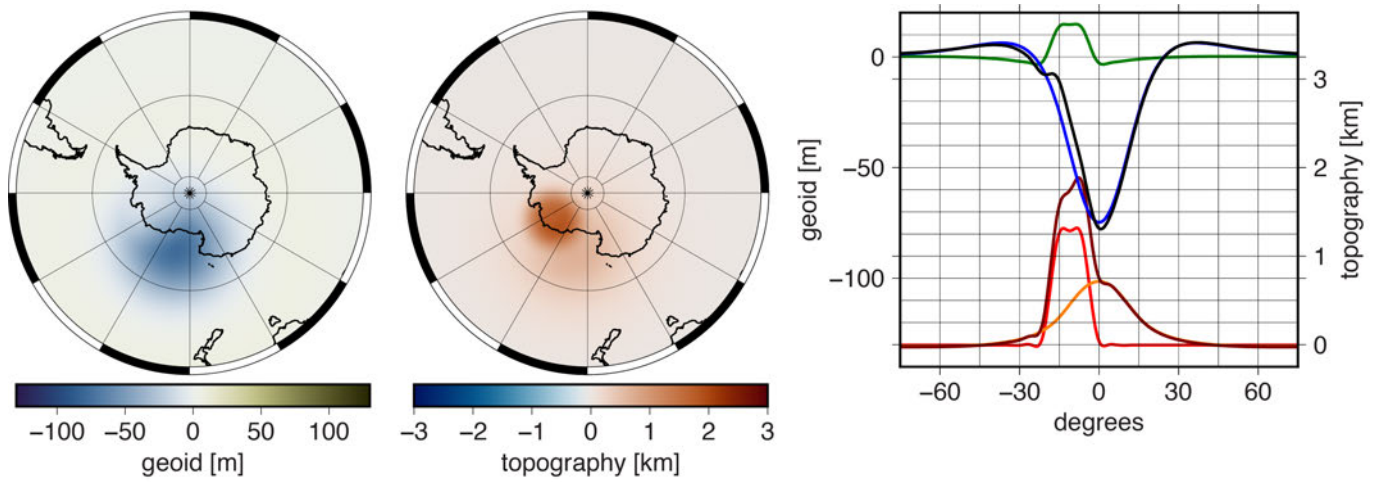


Figure 10 – Left and middle: Geoid and dynamic topography for a combination of two disks with -1% density anomaly: Upper disk in the depth range 100-250 km with 7.5 degrees of arc radius (cosbell smoothing from 3.75 to 11.25 degrees) and center at 77° S, 126° W, lower disk in the depth range 700-1000 km with 11 degree of arc radius (cosbell smoothing from 5.5 to 16.5 degrees) at 72° S, 165° W. **Right:** Profiles of geoid (green: upper disk; blue: lower disk; black: total) and dynamic topography (light red: upper disk; orange: lower disk; dark red: total) across centers of disks.

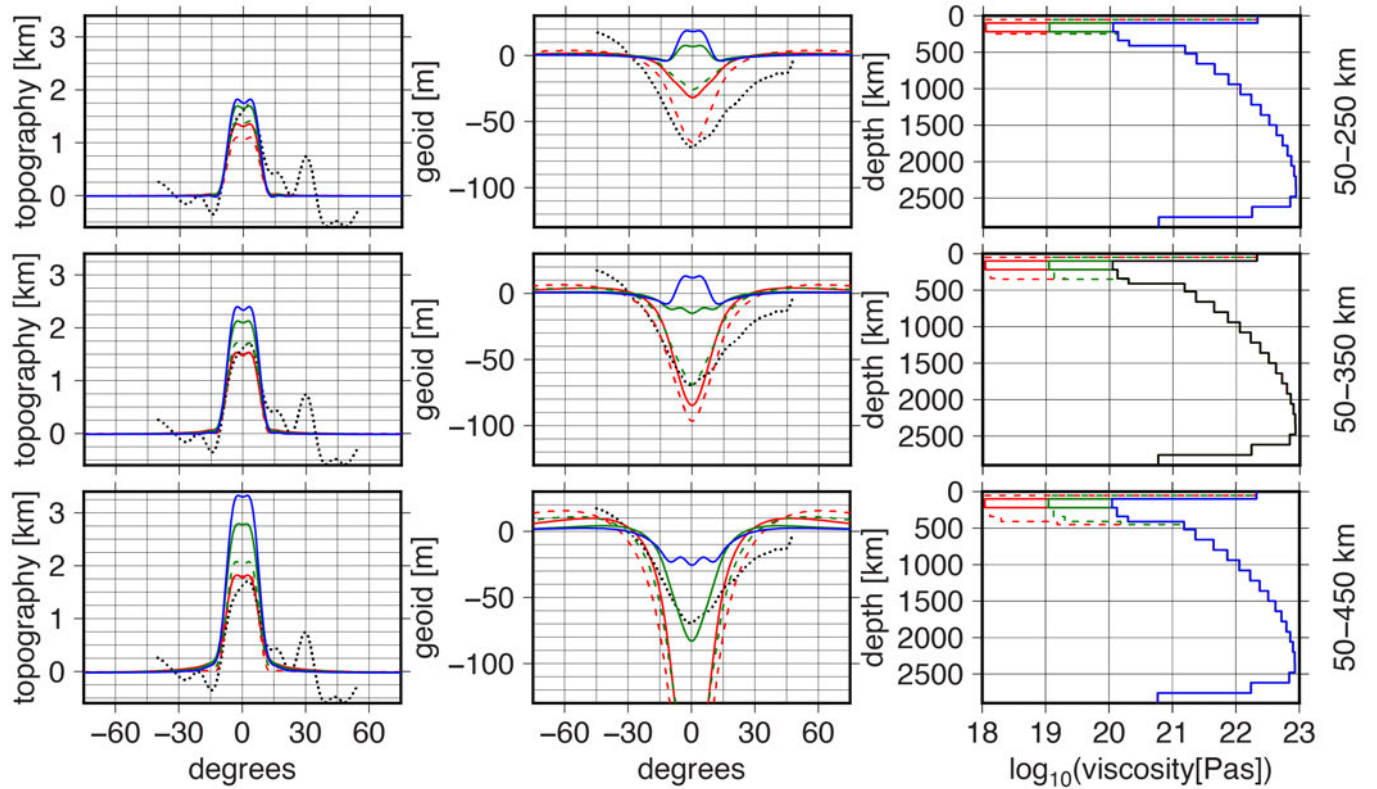


Figure 11 – Predicted dynamic topography (left) and geoid (center) for different viscosity structures (right). Computations are for disks of -1% density anomaly in the depth range 450 - 50 km (bottom), 350 - 50 km (middle) and 250 - 50 km (top); 8 degrees of arc radius with cosbell smoothing from 4 to 12 degrees. Viscosity is either the same as in Figures 8 and 9 (blue line) or reduced by factor 10 (green) or 100 (red) in the depth range 100-220 km (continuous) or in the same depth range as the disk (dashed). In the latter case, also the top (i.e., lithosphere) viscosity layer is reduced to 50 km thickness. Dotted lines are observation-based residual topography and geoid (curve 3 from Figure 3, with lower mantle contribution removed).

with 10 degrees of arc (converted to 1042 km), and 300 K maximum anomaly. For the radial viscosity, we chose the “red” profile, but with the increase of viscosity in the lithosphere explicitly included (purple dots in Figure 5) instead of a temperature decrease in the lithosphere. The radial extent of the anomaly is either 150-650 km (corresponding to

the reference case) or 50-350 km (corresponding to the best-fit case in Figure 11). For each disk we consider two cases with temperature dependence of viscosity, corresponding to the blue and green curve in Figure 5 (left graph). This leads to about a factor 6 viscosity decrease within the anomaly, according to equation 4, for the blue curve. For the

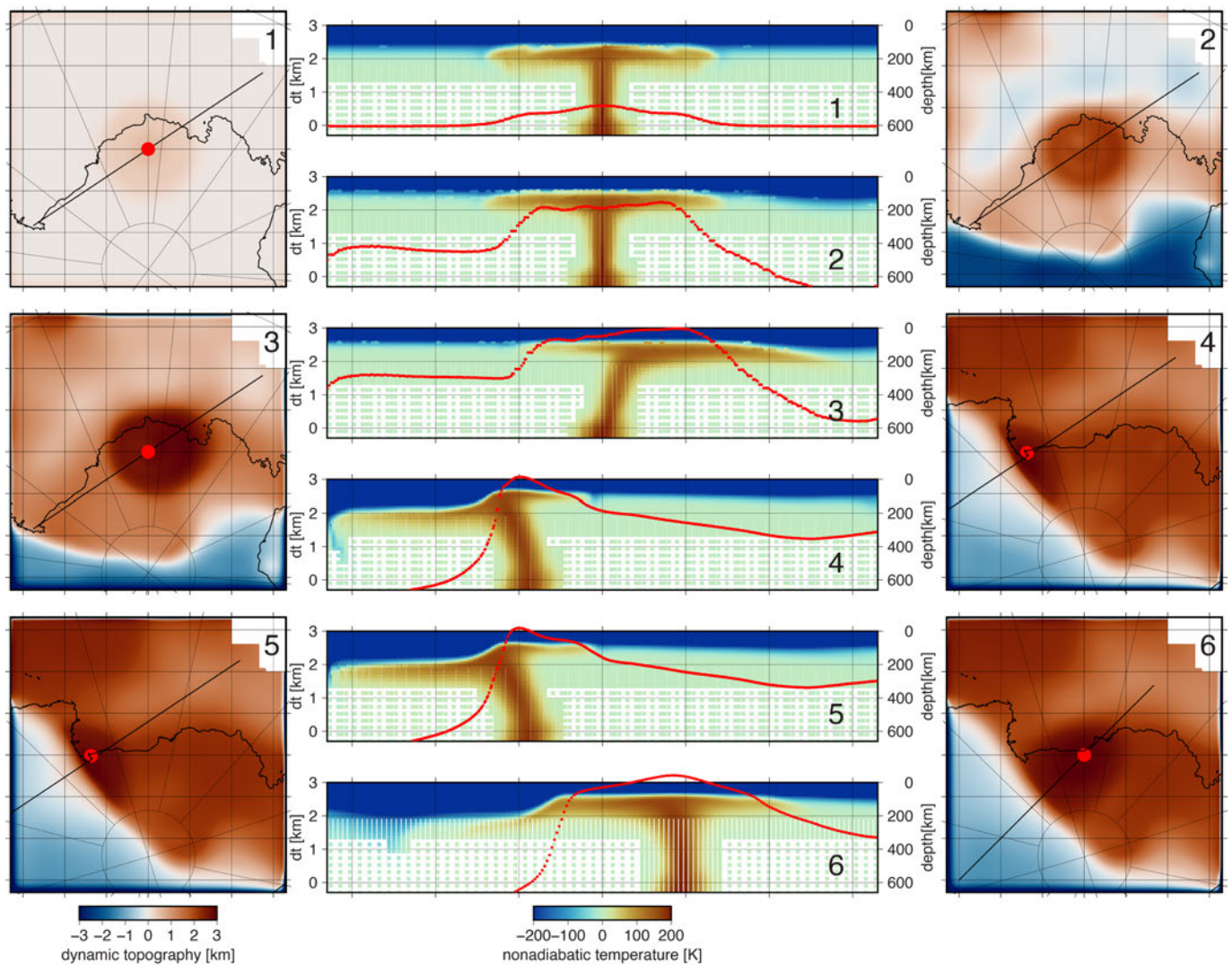


Figure 12 – ASPECT results, cases 1-6. Map views show computed dynamic topography, plume source locations (red dots), coastlines, profiles along which non-adiabatic temperature and dynamic topography (“dt”, lines of red dots) is plotted. Profiles are chosen such that they approximately cross both the centers of the plume source and the plume head. Note that cases 1-3 correspond to different geographic location of model box.

green curve, mostly the lower viscosity cutoff 10^{19} Pas (about factor 30-60 decrease) is reached. In the third case, only radial viscosity variations are considered. For the 150-650 km disk, dynamic topography has an amplitude of maximum vs. far field of 2819 m without lateral viscosity variations, 2564 m with the weak temperature dependence and 2511 m with the strong dependence. For the 50-350 km disk corresponding numbers are 2561 m, 2443 m and 2255 m, i.e., the reduced viscosity leads to at most 12% reduced dynamic topography amplitude. This amount is even less than what *Ghosh et al. (2010)* found – that lateral viscosity variations can affect dynamic topography by up to ~20 %.

With the estimate given in the methods section for a wavelength $\lambda = 3126$ km (width of the anomaly including cosine taper) in both x and y direction, the geoid due to dynamic topography should be about 5 % of dynamic topography itself. Thus, dynamic topography reduced by 118-308 m corresponds to about 6-15 m of additional geoid low. For example,

for our reference case we would obtain a geoid low of about 98-100 m instead of 85 m, closer to what is observed. To explain the 70 m geoid low which we attribute to upper mantle low-density materials, a somewhat smaller density anomaly, or a smaller depth extent of the anomaly, would be sufficient. So considering lateral viscosity variations can somewhat improve the joint fit of geoid and dynamic topography. Similarly, our synthetic results with reduced upper mantle viscosity also give a reduced dynamic topography and increased negative geoid anomaly, but to an even larger extent.

4 Discussion

Our results show that the geoid can be separated into a broad 60-m low from lower mantle slab superimposed to a smaller-scale 70-m low from upper-mantle low-density anomalies. This also broadly matches with *Spasojevic et al. (2010a)* who find that only 40% of the geoid low remains once the upwellings are removed in the upper 1000 km.

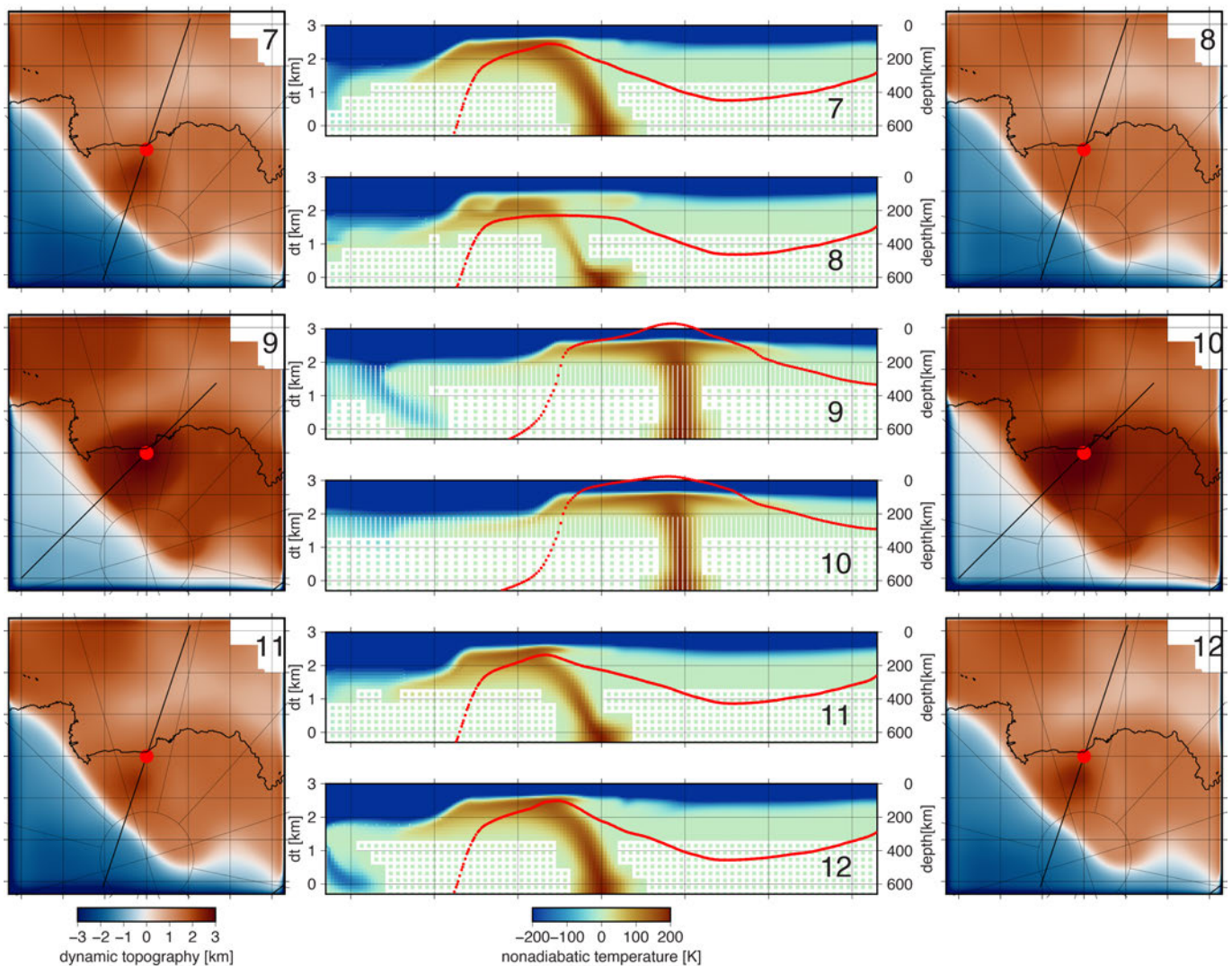


Figure 13 – ASPECT results, cases 7-12. Further explanations see Figure 12.

They suggest that this mode of upwelling in the mid-to-upper mantle is caused by buoyant hydrated mantle that was created by processes around and above subducted slabs.

We have conducted here simple analytical computations to address the question which depth range and size of a temperature anomaly beneath West Antarctica is required to explain the upper-mantle portion of the geoid low, as well as the residual topography high, and at the same time compatible with seismic tomography. In terms of our simple models, we find a reasonable fit for a 1% anomaly in a cylindrical disk of 10 degrees of arc radius, in the depth range 150 to 650 km if we use a “global” viscosity structure. However, with reduced viscosity in the uppermost mantle, a similar fit can be achieved for a disk in the 50-350 km depth range.

The observed geoid low is somewhat larger in extent than the residual topography high. This is also the case for the modelled geoid vs. topography, but even compared to that difference, the observed geoid is disproportionately large. But if the geoid contribution due to slabs and LLSVPs is taken into

account (Figure 7D) the remaining geoid anomaly has approximately the right size.

The observed geoid low is centered on the Ross Sea, whereas the residual topography high is centered on West Antarctica, further to the southeast. This could indicate a density anomaly tilted towards southeast, centered below Ross Sea at greater depth and below West Antarctica at more shallow depth. In order to assess whether such a tilt is supported by tomography, and since there are quite some differences between individual tomography models we first use Submachine (*Hosseini et al., 2018*) to look at an average of six P-wave models (only choosing those that show some structure in this region and avoiding similar models from the same group: PRI-S05, DETOX-P1, GAP-P4, LLNL-G3Dv3, MIT_USA_2016MAY, UU-P07). We find that this average shows a very localized low of about -1% and about 500 km across at 200 km depth, and somewhat larger at 400 km, centered on the southwestern Ross Sea near Mount Erebus and also near the center of the geoid low. We then look at an average of nine S-wave models chosen by the same criteria (3D2016_09Sv, HMSL-S06, PRI-S05, TX2019slab-S,

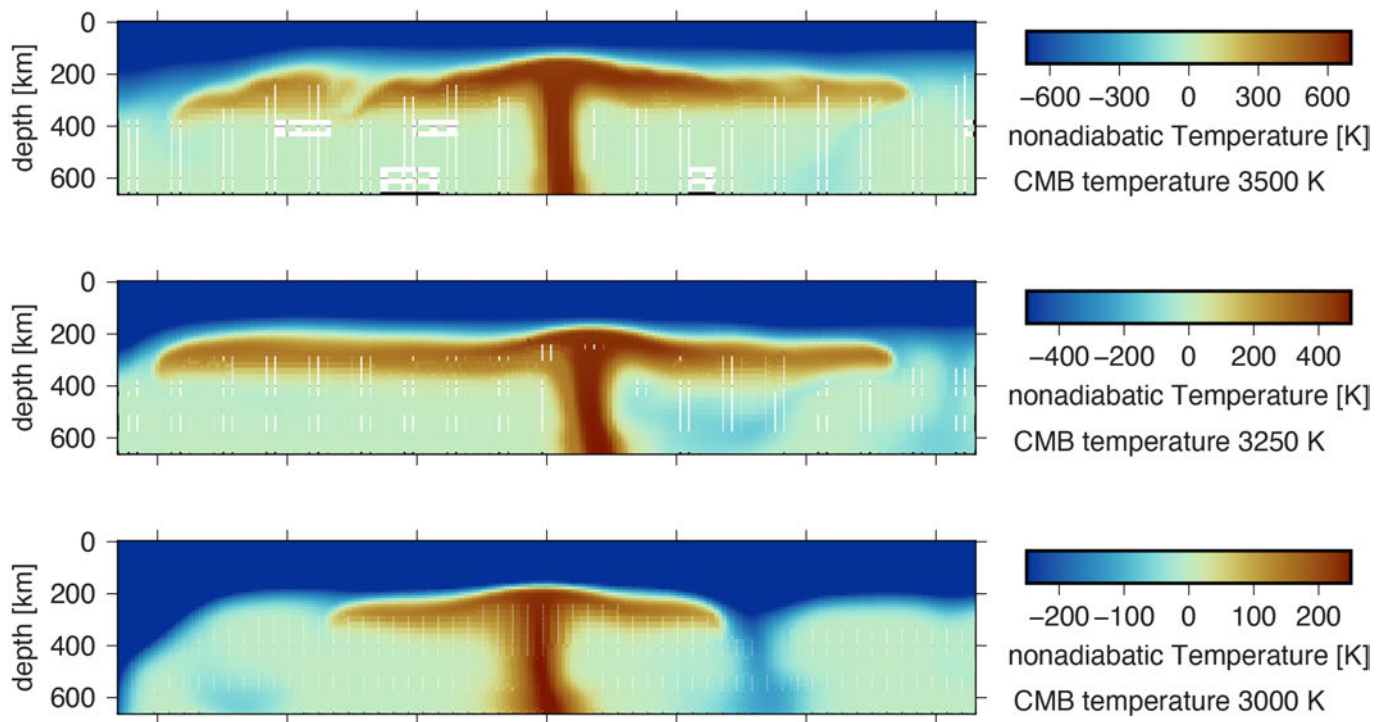


Figure 14 – ASPECT results computed for whole mantle box but only shown for the upper mantle, with CMB temperatures 3000 K, 3250 K, 3500 K. Note the different color scale for different cases. cross-sections are chosen such that they approximately pass through the center of the plume conduit at all depths in the upper mantle. Times are 30 Myr after the plume head reaches the base of the lithosphere, which is 249 Myr after model initiation for 3500 K, 390 Myr for 3250 K and 323 Myr for 3000 K.

SAW642ANb, SEISGLOB2, SEMUCB-WM1, SEMum, SL2013sv): At 200 km depth, there is an anomaly over the entire Ross Sea, whereas at 100 km depth it also extends across West Antarctica where the residual topography high is centered. This is also similar to the map in Figure 1A. Considering S-wave models at shallower depth and P-wave models at greater depth is warranted, since also surface waves can be used to construct S-wave models. These results hence indicate that the plume anomaly becomes wider closer to the surface - similar to our dynamic models - and is tilted towards East.

However, the structure seen in tomography model ANT-20 (Lloyd *et al.*, 2020), which is more reliable in that region, only partly agrees: down to about 200 km, it clearly shows two separate negative anomalies, approximately beneath Mount Erebus and beneath coastal West Antarctica (Marie Byrd Land) (see also Figure 1). These anomalies continue, but get weaker with depth, and really become part of negative larger anomalies that continue beneath the Southern Ocean. Only beneath West Antarctica, a continuation to the lower mantle is indicated.

In contrast, the dynamic models with a plume rising beneath Mount Erebus rather predict a tilt towards the West. If the plume location is shifted eastward, near the eastern end of the Ross Shelf edge, then the plume tilt is towards SSW for flow model TD, and there is very little tilt for flow model C. Only for a plume location even further East, beneath West Antarctica, the dynamical models yield a tilt towards

the East. Hence the dynamic plume models match both the vote maps and tomography model ANT-20 quite poorly.

Another possible cause (or contributor) for the offset between dynamic topography maximum and geoid minimum could be lithospheric thickness variations: The lithosphere in West Antarctica appears to be even thinner than the oceanic lithosphere beneath Ross Sea (Figure 1), hence the plume could reach closer to the surface, and cause stronger dynamic topography, beneath West Antarctica, whereas these shallower plume materials have little effect on the geoid. Finally, the spatial shift between the inferred upper mantle geoid and the topography signals could also be partially due to an imperfect correction for the deep slab signal: Given uncertainties in the reference frame for the Mesozoic, subducted slabs could be easily shifted by about 10 degrees. In this case, the subducted slabs (see e.g., Bredow *et al.*, 2023, Figure 1) and the corresponding geoid low (Figure 7C) could be shifted towards Ross Sea, such that the remaining geoid low (Figure 7D) could be shifted towards West Antarctica. However, without proper modelling, this remains a qualitative assumption as the lowest part of the geoid low in Ross Sea is quite narrow and pointed, which would rather suggest an upper mantle origin.

A somewhat different approach is taken by Spasojevic *et al.* (2010b): They model both geoid and dynamic topography by a combination of negative, upwelling density anomaly overlying a positive,

downwelling anomaly. In this way, they are also able to explain a localized geoid low, but by considering time evolution, they can additionally match the subsidence history of Campbell Plateau.

Dynamic forward models always yield a spreading of the plume at shallower levels. Similarly, tomography models also tend to show stronger anomalies closer to the surface, but they still tend to show anomalously slow material (although with a lower amplitude) down to a depth of about 1000 km. In contrast, the dynamic models show basically no anomaly at all below depth ~ 300 km. Accordingly, density models based on tomography can approximately explain the pattern of geoid and dynamic topography, and the discrepancy in amplitude (compare e.g., Figures 3 and 4) with dynamic topography amplitude over-predicted and geoid amplitude under-predicted could be at least partly due to lateral viscosity variations (as discussed above).

The results shown for the dynamic models correspond to a time ~ 30 Myr after the plume head reaches the surface. A deeper anomaly could result if the plume is just rising to the surface, but this is at odds with volcanism in West Antarctica occurring since ~ 30 Ma. We don't expect that large amounts of plume material would stay in or below the transition zone, unless somehow the thermal buoyancy is balanced by a negative chemical (or phase boundary) buoyancy, but overall neutrally buoyant plume material would have no effect on geoid and dynamic topography. One possible explanation could be a pulsating plume, with a new buoyant pulse just having reached transition zone depths. Our dynamical modelling is purely thermal, and compositional variations could cause plume pulsations (*Lin and van Keken, 2006a,b; Heyn et al., 2020*) and more complicated morphology (*Farnetani and Samuel, 2005; Kumagai et al., 2008*).

The shallow disk predicted in our dynamic forward models can approximately explain dynamic topography, but with our dynamic forward modelling approach we cannot directly compute the geoid. Instead, we approximate the plume spreading at shallow levels by a cylindrical disk, for which we compute geoid and dynamic topography analytically with the spherical harmonics approach. With a viscosity structure that corresponds to global average (approximately 10^{20} Pa s viscosity minimum below the lithosphere) the cylindrical disk required to match geoid and dynamic topography is deeper than in the dynamic forward models. However, with viscosity reduced in parts of the upper mantle, for example 10 times between 350 and 50 km depth or 100 times between 220 and 100 km depth, we can get a better fit for a shallower disk, e.g., 8 degrees radius between 50 and 350 km depth.

This is still a somewhat larger depth extent than what our dynamic forward models typically yield. We can only speculate, why there seems to be

such a large "pool" of low-density material below West Antarctica, causing such a large negative geoid, whereas this does not appear to be the case for other plumes or plume candidates. One possible reason could be that Antarctica has been nearly stationary for a long time in Earth history. Also, being located inbetween the two upwellings associated with the Pacific and African LLSVP there is perhaps not a very strong upper mantle flow. Furthermore, there could be an "insulating" effect of the continent. These reasons could allow the plume material to accumulate, whereas for other plumes it might be dragged away by the plate (e.g., for Hawaii) or pushed away by upper mantle flow (e.g., East Africa or Iceland). Another difference is that the predicted source location at the CMB is not above an LLSVP. Hence it might be that this plume has a strong thermal buoyancy, whereas for other plumes, buoyancy is reduced as they entrain chemically different materials from the LLSVPs.

With respect to the initially posed question of how fast uplift may occur following melting of ice sheets, the implications of our results regarding mantle viscosity are important. A density anomaly of 1% as we found appropriate for our cylinder models, when combined with a thermal expansivity of about $2.5 \cdot 10^{-5}/K$ corresponds to about 400 K temperature anomaly. However, as discussed above, the anomaly may be somewhat less if it extends somewhat deeper than modelled here, and/or if the effect of lateral viscosity variations on geoid and topography are considered. Hence 300 K would appear a more realistic estimate, still on the upper bound of what is inferred from petrology (*Herzberg and Gazel, 2009*). With our lower estimate for rH/R from Figure 5 we estimated a viscosity reduction by a factor 7. With the upper limit $r = 1$ (corresponding to diffusion creep), rH/R could be around 80,000 K, and we get a reduction by a factor ~ 570 . Given that 300 K is still on the high end of temperature anomaly estimates, we can say that our best estimate is "one or two orders of magnitude" viscosity decrease. Given that the global average of viscosity just below the lithosphere is about 10^{20} Pas or somewhat higher (*Steinberger, 2016*), our results are consistent with a viscosity minimum beneath West Antarctica somewhere around $10^{18} - 10^{19}$ Pas, but viscosity increasing with depth. We also find that, for such low viscosities in the upper part of the upper mantle, we can get a better fit of geoid and dynamic topography, even if the density anomaly only extends to depth 350 km, approximately consistent with our geodynamic forward model results. As this viscosity range is still rather large and uncertain, we cannot provide an independent viscosity estimate, but at least lend support to other recent estimates (*Ivins et al., 2022; van der Wal et al., 2022*) which are similar or somewhat higher.

5 Conclusions

We have discussed here models of mantle structure beneath West Antarctica constrained by geoid and residual topography. We find that these can be best explained if there is underlying low-density material in the upper mantle, and possibly the uppermost part of the lower mantle. In order to explain the sizable geoid low, this anomaly needs to be quite large, reaching about 2000 km in lateral extent and several hundred km radially, with a magnitude of about -1% or somewhat less. With a radial viscosity structure that is appropriate for global average, an anomaly that is concentrated in the uppermost mantle beneath the lithosphere is insufficient to explain the geoid low, and tends to yield a comparatively large dynamic topography. However, if viscosities are reduced by a factor 10-100 in the uppermost mantle, rather shallow density anomalies that are similar to or extending only slightly deeper than the spreading stationary plume head in our time-dependent dynamic models could be sufficient to explain both geoid and dynamic topography. The most likely explanation for the low densities are higher temperatures (perhaps by about 300 K), leading to lower viscosities. Our best estimate for viscosity just below the West Antarctic lithosphere is about $10^{18} - 10^{19}$ Pas.

Acknowledgements

This work was partially funded by the Research Council of Norway Centre of Excellence Project 223272. Additional funding was provided from the innovation pool of the Helmholtz Association through the Advanced Earth System Modelling Capacity (ESM) activity. We thank the Computational Infrastructure for Geodynamics (geodynamics.org) which is funded by the National Science Foundation under award EAR-0949446 and EAR-1550901 for supporting the development of ASPECT. We thank Thorsten Becker and Eivind Straume for providing tomography models and plate reconstructions in spherical harmonic format. Models 1-3 were performed on resources provided by Sigma2 - the National Infrastructure for High Performance Computing and Data Storage in Norway. Remaining computations were performed with resources provided by the North-German Supercomputing Alliance (HLRN). We thank for detailed and constructive reviews provided by Jacqueline Austermann and Isabelle Panet.

Author contributions

B.S. conceived and wrote the paper. Computations were performed and figures were created by **B.S.**, **M.G.** and **R.L.**

Data availability

The version of the ASPECT code that was used to carry out the modelling

presented in this work can be obtained at <https://doi.org/10.5281/zenodo.8417383>.

The input parameter files (.prm) and required data to reproduce the modelling results are available at <https://doi.org/10.5880/GFZ.2.5.2023.004>.

Competing interests

The authors declare no competing interests.

Peer review

This publication was peer-reviewed by Jacqueline Austermann and Isabelle Panet. The full peer-review report can be found here: <https://doi.org/10.5880/GFZ.2.5.2023.004>.

Copyright notice

© Author(s) 2023. This article is distributed under the [Creative Commons Attribution 4.0 International License](https://creativecommons.org/licenses/by/4.0/), which permits unrestricted use, distribution, and reproduction in any medium, provided the original author(s) and source are credited, and any changes made are indicated.

References

- A, G., J. Wahr, and S. Zhong (2012), Computations of the viscoelastic response of a 3-D compressible Earth to surface loading: an application to Glacial Isostatic Adjustment in Antarctica and Canada, *Geophysical Journal International*, 192(2), 557–572, doi: 10.1093/gji/ggs030.
- Accardo, N. J., D. A. Wiens, S. Hernandez, R. C. Aster, A. Nyblade, A. Huerta, S. Anandakrishnan, T. Wilson, D. S. Heeszel, and I. W. D. Dalziel (2014), Upper mantle seismic anisotropy beneath the West Antarctic Rift System and surrounding region from shear wave splitting analysis, *Geophysical Journal International*, 198(1), 414–429, doi: 10.1093/gji/ggu117.
- An, M., D. Wiens, Y. Zhao, M. Feng, A. Nyblade, M. Kanao, Y. Li, A. Maggi, and J.-J. Lévesque (2015a), Temperature, lithosphere-asthenosphere boundary, and heat flux beneath the Antarctic Plate inferred from seismic velocities, *Journal of Geophysical Research: Solid Earth*, 120, 8720–8742, doi: 10.1002/2015JB011917.
- An, M., D. Wiens, Y. Zhao, M. Feng, A. Nyblade, M. Kanao, Y. Li, A. Maggi, and J.-J. Lévesque (2015b), S-velocity model and inferred Moho topography beneath the Antarctic Plate from Rayleigh waves, *Journal of Geophysical Research: Solid Earth*, 120, 359–383, doi: 10.1002/2014JB011332.
- Artemieva, I. M. (2022), Antarctica ice sheet basal melting enhanced by high mantle heat, *Earth-Science Reviews*, 226, 103954, doi: 10.1016/j.earscirev.2022.103954.
- Austermann, J., D. Pollard, J. X. Mitrovica, R. Moucha, A. M. Forte, R. M. DeConto, D. B. Rowley, and M. E. Raymo (2015), The impact of dynamic topography change on Antarctic ice sheet stability during the mid-Pliocene warm period, *Geology*, 43(10), 927–930, doi: 10.1130/G36988.1.

- Bangerth, W., J. Dannberg, M. Fraters, R. Gassmoeller, A. Glerum, T. Heister, and J. Naliboff (2021a), ASPECT v2.3.0, doi: 10.5281/zenodo.5131909.
- Bangerth, W., J. Dannberg, M. Fraters, R. Gassmoeller, A. Glerum, T. Heister, and J. Naliboff (2021b), ASPECT: Advanced Solver for Problems in Earth's Convection, User Manual, doi: 10.6084/m9.figshare.4865333.
- Bao, X., C. Lithgow-Bertelloni, M. Jackson, and B. Romanowicz (2022), On the relative temperatures of Earth's volcanic hotspots and mid-ocean ridges, *Science*, 375, 57–61, doi: 10.1126/science.abj8944.
- Barletta, V. R., M. Bevis, B. E. Smith, T. Wilson, A. Brown, A. Bordoni, M. Willis, S. A. Khan, M. Rovira-Navarro, I. Dalziel, R. Smalley, E. Kendrick, S. Konfal, D. J. Caccamise, R. C. Aster, A. Nyblade, and D. A. Wiens (2018), Observed rapid bedrock uplift in Amundsen Sea Embayment promotes ice-sheet stability, *Science*, 360(6395), 1335–1339, doi: 10.1126/science.aao1447.
- Behrendt, J. C., W. E. LeMasurier, A. K. Cooper, F. Tessensohn, A. Trehu, and D. Damaske (1991), Geophysical studies of the West Antarctic rift system, *Tectonics*, 10, 1257–1273.
- Behrendt, J. C., W. LeMasurier, and A. K. Cooper (1992), The West Antarctic rift system, a propagating rift "captured" by a mantle plume, in: *Recent Progress in Antarctic Earth Science*, edited by K. Yoshida, K. Kaminuma and K. Shiraishi, *Terra Science, Tokyo*, pp. 315–322.
- Blank, B., V. Barletta, H. Hu, F. Pappa, and W. van der Wal (2021), Effect of Lateral and Stress-Dependent Viscosity Variations on GIA Induced Uplift Rates in the Amundsen Sea Embayment, *Geochemistry, Geophysics, Geosystems*, 22(9), e2021GC009807, doi: 10.1029/2021GC009807.
- Bredow, E., B. Steinberger, R. Gassmüller, and J. Dannberg (2023), Mantle convection and possible mantle plumes beneath Antarctica - insights from geodynamic models and implications for topography, *Geological Society of London, Memoirs*, 56, 253–266, doi: 10.1144/M56-2020-2.
- Chambat, F., Y. Ricard, and B. Valette (2010), Flattening of the Earth: further from hydrostaticity than previously estimated, *Geophysical Journal International*, 183, 727–732, doi: 10.1111/j.1365-246X.2010.04771.x.
- Chase, C. G., and D. R. Sprowl (1983), The modern geoid and ancient plate boundaries, *Earth and Planetary Science Letters*, 62, 314–320, doi: 10.1016/0012-821X(83)90002-X.
- Christensen, U. R. (1983), Convection in a variable-viscosity fluid: Newtonian versus power-law rheology, *Earth and Planetary Science Letters*, 64, 153–162, doi: 10.1016/0012-821X(83)90060-2.
- Cooper, A. F., L. J. Adam, R. F. Coulter, G. N. Eby, and W. C. McIntosh (2007), Geology, geochronology and geochemistry of a basanitic volcano, White Island, Ross Sea, Antarctica, *Journal of Volcanology and Geothermal Research*, 165(3), 189–216, doi: 10.1016/j.jvolgeores.2007.06.003.
- Cramer, F. (2018), Scientific colour maps, *Zenodo*, doi: 10.5281/zenodo.1243862.
- Cui, R., J. Fang, and Y. Wang (2022), Effect of Mantle Viscosity Structures on Simulations of Geoid Anomalies in the Ross Sea Area, *Pure and Applied Geophysics*, 179, 2841–2850, doi: 10.1007/s00024-022-03081-1.
- DeConto, R. M., and D. Pollard (2003), Rapid Cenozoic glaciation of Antarctica induced by declining atmospheric CO₂, *Nature*, 421, 245–249, doi: 10.1038/nature01290.
- Dobrovine, P. V., B. Steinberger, and T. H. Torsvik (2012), Absolute plate motions in a reference frame defined by moving hotspots in the Pacific, Atlantic and Indian oceans, *Journal of Geophysical Research*, 117, B09101, doi: 10.1029/2011JB009072.
- Emry, E. L., A. A. Nyblade, J. Julià, S. Anandakrishnan, R. C. Aster, D. A. Wiens, A. D. Huerta, and T. J. Wilson (2015), The mantle transition zone beneath West Antarctica: Seismic evidence for hydration and thermal upwellings, *Geochemistry, Geophysics, Geosystems*, 16, 40–58, doi: 10.1002/2014GC005588.
- Farnetani, C. G., and H. Samuel (2005), Beyond the thermal plume paradigm, *Geophysical Research Letters*, 32(7), L07311, doi: 10.1029/2005GL022360.
- Fisher, A. T., K. D. Mankoff, S. M. Tulaczyk, S. W. Tyler, N. Foley, and the WISSARD Science Team (2015), High geothermal heat flux measured below the West Antarctic Ice Sheet, *Science Advances*, 1, e150009, doi: 10.1126/sciadv.1500093.
- Fox Maule, C., M. C. Purucker, N. Olsen, and K. Mosegaard (2005), Heat flux anomalies in Antarctica revealed by satellite magnetic data, *Science*, 309, 464–467, doi: 10.1126/science.1106888.
- Garbe, J., T. Albrecht, A. Levermann, J. F. Donges, and R. Winkelmann (2020), The hysteresis of the Antarctic Ice Sheet, *Nature*, 585, 538–544.
- Gassmüller, R., J. Dannberg, E. Bredow, B. Steinberger, and T. H. Torsvik (2016), Major influence of plume-ridge interaction, lithosphere thickness variations, and global mantle flow on hotspot volcanism—the example of Tristan, *Geochemistry, Geophysics, Geosystems*, 17(4), 1454–1479, doi: 10.1002/2015GC006177.
- Ghosh, A., T. W. Becker, and S. J. Zhong (2010), Effects of lateral viscosity variations on the geoid, *Geophysical Research Letters*, 37, L01301, doi: 10.1029/2009GL040426.
- Grand, S. P. (2002), Mantle shear-wave tomography and the fate of subducted slabs, *Philosophical Transactions of the Royal Society London A*, 360, 2475–2491, doi: 10.1098/rsta.2002.1077.
- Gubanov, A. P., and W. D. Mooney (2009), New global maps of crustal basement age, *Eos Transactions of the American Geophysical Union*, 90, Fall Meet. Suppl., Abstract T53B-1583.
- Hager, B. H., and R. J. O'Connell (1979), Kinematic models of large-scale flow in the Earth's mantle, *Journal of Geophysical Research*, 84, 1031–1048, doi: 10.1029/JB084iB03p01031.
- Hager, B. H., and R. J. O'Connell (1981), A simple global model of plate dynamics and mantle convection, *Journal of Geophysical Research*, 86, 4843–4867, doi: 10.1029/JB086iB06p04843.
- Hansen, S. E., J. H. Graw, L. M. Kenyon, A. A. Nyblade, D. A. Wiens, R. C. Aster, A. D. Huerta, S. Anandakrishnan, and T. Wilson (2014), Imaging the Antarctic mantle using adaptively parameterized P-wave tomography: Evidence for heterogeneous structure beneath West Antarctica, *Earth and Planetary Science Letters*, 408, 66–78, doi: 10.1016/j.epsl.2014.09.043.
- Hay, C. C., H. C. P. Lau, N. Gomez, J. Austermann, E. Powell, J. X. Mitrovica, K. Letychev, and D. A. Wiens (2017), Sea level fingerprints in a region of complex Earth structure: The case of WAIS, *Journal of Climate*, 30(6), 1881–1892, doi: 10.1175/JCLI-D-16-0388.1.

- Heister, T., J. Dannberg, R. Gassmüller, and W. Bangerth (2017), High accuracy mantle convection simulation through modern numerical methods. II: Realistic models and problems, *Geophysical Journal International*, 210(2), 833–851, doi: 10.1093/gji/ggx195.
- Herzberg, C., and E. Gazel (2009), Petrological evidence for secular cooling in mantle plumes, *Nature*, 458, 619–622, doi: 10.1038/nature07857.
- Heyn, B. H., C. P. Conrad, and R. G. Trønnes (2020), How thermochemical piles can (periodically) generate plumes at their edges, *Journal of Geophysical Research: Solid Earth*, 125(6), e2019JB018726, doi: 10.1029/2019JB018726.
- Hole, M. J., and W. E. LeMasurier (1994), Tectonic controls on the geochemical composition of Cenozoic, mafic alkaline volcanic rocks from West Antarctica, *Contributions to Mineralogy and Petrology*, 117, 187–202, doi: 10.1007/BF00286842.
- Hosseini, K., K. J. Matthews, K. Sigloch, G. E. Shephard, M. Domeier, and M. Tsekhmistrenko (2018), SubMachine: Web-Based tools for exploring seismic tomography and other models of Earth's deep interior, *Geochemistry, Geophysics, Geosystems*, 19, 1464–1483, doi: 10.1029/2018GC007431.
- Ivins, E. R., W. van der Wal, D. A. Wiens, A. J. Lloyd, and L. Caron (2022), Antarctic upper mantle rheology, *Geological Society of London, Memoirs*, 56, 267–294, doi: 10.1144/M56-2020-19.
- Kaufmann, G., P. Wu, and E. R. Ivins (2005), Lateral viscosity variations beneath Antarctica and their implications on regional rebound motions and seismotectonics, *Journal of Geodynamics*, 39(2), 165–181, doi: 10.1016/j.jog.2004.08.009.
- Kennett, J. P. (1977), Cenozoic evolution of Antarctic glaciation, the circum-Antarctic oceans and their impact on global paleoceanography, *Journal of Geophysical Research*, 82, 3843–3859.
- King, M. A., P. L. Whitehouse, and W. van der Wal (2015), Incomplete separability of Antarctic plate rotation from glacial isostatic adjustment deformation within geodetic observations, *Geophysical Journal International*, 204(1), 324–330, doi: 10.1093/gji/ggv461.
- Kronbichler, M., T. Heister, and W. Bangerth (2012), High accuracy mantle convection simulation through modern numerical methods, *Geophysical Journal International*, 191, 12–29, doi: 10.1111/j.1365-246X.2012.05609.x.
- Kumagai, I., A. Davaille, K. Kurita, and E. Stutzmann (2008), Mantle plumes: Thin, fat, successful, or failing? constraints to explain hot spot volcanism through time and space, *Geophysical Research Letters*, 35(16), L16301, doi: 10.1029/2008GL035079.
- Kyle, P. R., J. A. Moore, and M. F. Thirlwall (1992), Petrologic Evolution of Anorthoclase Phonolite Lavas at Mount Erebus, Ross Island, Antarctica, *Journal of Petrology*, 33, 849–875, doi: 10.1093/petrology/33.4.849.
- Laske, G., G. Masters, Z. Ma, and M. Pasyanos (2013), Update on CRUST1.0 - A 1-degree Global Model of Earth's Crust, in *EGU General Assembly Conference Abstracts*, EGU General Assembly Conference Abstracts, pp. EGU2013–2658.
- Lau, H. C. P., J. Austermann, B. K. Holtzman, C. Havlin, A. J. Lloyd, C. Book, and E. Hopper (2021), Frequency dependent mantle viscoelasticity via the complex viscosity: Cases from Antarctica, *Journal of Geophysical Research: Solid Earth*, 126(11), e2021JB022,622, doi: 10.1029/2021JB022622.
- Lear, C. H., H. Elderfield, and P. A. Wilson (2000), Cenozoic deep-sea temperatures and global ice volumes from Mg/Ca in benthic foraminiferal calcite, *Science*, 287, 269–272, doi: 10.1126/science.287.5451.269.
- LeMasurier, W. (2013), Shield volcanoes of Marie Byrd Land, West Antarctic rift: oceanic island similarities, continental signature, and tectonic controls, *Bulletin of Volcanology*, 75, 726, doi: 10.1007/s00445-013-0726-1.
- LeMasurier, W. E., and D. C. Rex (1989), Evolution of linear volcanic ranges in Marie Byrd Land, West Antarctica, *Journal of Geophysical Research: Solid Earth*, 94(B6), 7223–7236, doi: 10.1029/JB094iB06p07223.
- Lenton, T. M., H. Held, E. Kriegler, J. W. Hall, W. Lucht, S. Rahmstorf, and H. J. Schellnhuber (2008), Tipping elements in the Earth's climate system, *Proceedings of the National Academy of Sciences*, 105(6), 1786–1793, doi: 10.1073/pnas.0705414105.
- Lin, S.-C., and P. E. van Keken (2006a), Dynamics of thermochemical plumes: 1. plume formation and entrainment of a dense layer, *Geochemistry, Geophysics, Geosystems*, 7(2), Q02006, doi: 10.1029/2005GC001071.
- Lin, S.-C., and P. E. van Keken (2006b), Dynamics of thermochemical plumes: 2. complexity of plume structures and its implications for mapping mantle plumes, *Geochemistry, Geophysics, Geosystems*, 7(3), Q03003, doi: 10.1029/2005GC001072.
- Lloyd, A. J., D. A. Wiens, H. Zhu, J. Tromp, A. A. Nyblade, R. C. Aster, S. E. Hansen, I. W. D. Dalziel, T. J. Wilson, E. R. Ivins, and J. P. O'Donnell (2020), Seismic structure of the Antarctic upper mantle imaged with adjoint tomography, *Journal of Geophysical Research: Solid Earth*, 125, doi: 10.1029/2019JB017823.
- Lobanov, S. S., S. Speziale, and S. Brune (2021), Modelling Mie scattering in pyrolite in the laser-heated diamond anvil cell: Implications for the core-mantle boundary temperature determination, *Physics of the Earth and Planetary Interiors*, 318, 106773, doi: 10.1016/j.pepi.2021.106773.
- Lu, C., S. P. Grand, H. Lai, and E. J. Garnero (2019), TX2019slab: A new P and S tomography model incorporating subducting slabs, *Journal of Geophysical Research*, 124, 11,549–11,567, doi: 10.1029/2019JB017448.
- Martos, Y. M., M. Catalán, T. A. Jordan, A. Golynsky, D. Golynsky, G. Eagles, and D. G. Vaughan (2017), Heat flux distribution of Antarctica unveiled, *Geophysical Research Letters*, 44(22), 11,417–11,426, doi: 10.1002/2017GL075609.
- Müller, R. D., M. Sdrolias, C. Gaina, and W. R. Roest (2008), Age, spreading rates, and spreading asymmetry of the world's ocean crust, *Geochemistry, Geophysics, Geosystems*, 9, Q04,006, doi: 10.1029/2007GC001743.
- Nield, G. A., P. L. Whitehouse, W. van der Wal, B. Blank, J. P. O'Donnell, and G. W. Stuart (2018), The impact of lateral variations in lithospheric thickness on glacial isostatic adjustment in West Antarctica, *Geophysical Journal International*, 214(2), 811–824, doi: 10.1093/gji/ggy158.
- O'Donnell, J., K. Selway, A. Nyblade, R. Brazier, D. Wiens, S. Anandakrishnan, R. Aster, A. Huerta, T. Wilson, and J. Winberry (2017), The uppermost mantle seismic velocity and viscosity structure of central West Antarctica, *Earth and Planetary Science Letters*, 472, 38–49, doi: 10.1016/j.epsl.2017.05.016.

- Panter, K. S., and A. P. Martin (2022), West Antarctic mantle deduced from mafic magmatism, *Geological Society of London, Memoirs*, 56, 133–149, doi: 10.1144/M56-2021-10.
- Panter, K. S., P. Castillo, S. Krans, C. Deering, W. McIntosh, J. W. Valley, K. Kitajima, P. Kyle, S. Hart, and J. Blusztajn (2018), Melt origin across a rifted continental margin: a case for subduction-related metasomatic agents in the lithospheric source of alkaline basalt, NW Ross Sea, Antarctica, *Journal of Petrology*, 59(3), 517–558, doi: 10.1093/ptrology/egy036.
- Paul, H., and M. R. Kumar (2022), Strong influence of tomographic models on geoid prediction: Case studies from Indian Ocean and Ross Sea geoids, *Tectonophysics*, 836, 229429, doi: 10.1016/j.tecto.2022.229429.
- Pavlis, N. K., S. A. Holmes, S. C. Kenyon, and J. K. Factor (2012), The development and evaluation of the Earth Gravitational Model 2008 (EGM2008), *Journal of Geophysical Research*, 117, B04406, doi: 10.1029/2011JB008916.
- Pavoni, N. (1969), Zonen lateraler horizontaler Verschiebung in der Erdkruste und daraus ableitbare Aussagen zur globalen Tektonik, *Geologische Rundschau*, 59, 56–77.
- Pavoni, N. (1985), Pacific/anti-Pacific bipolarity in the structure of the Earth's mantle, *Eos Transactions of the American Geophysical Union*, 66, 497.
- Paxman, G. J. G. (2022), Antarctic palaeotopography, *Geological Society of London, Memoirs*, 56, 231–251, doi: 10.1144/M56-2020-7.
- Powell, E., N. Gomez, C. Hay, K. Latychev, and J. X. Mitrovica (2020), Viscous Effects in the Solid Earth Response to Modern Antarctic Ice Mass Flux: Implications for Geodetic Studies of WAIS Stability in a Warming World, *Journal of Climate*, 33(2), 443–459, doi: 10.1175/JCLI-D-19-0479.1.
- Powell, E. M., L. Pan, M. J. Hoggard, K. Latychev, N. Gomez, J. Austermann, and J. X. Mitrovica (2021), The impact of 3-D Earth structure on far-field sea level following interglacial West Antarctic Ice Sheet collapse, *Quaternary Science Reviews*, 273, 107256, doi: 10.1016/j.quascirev.2021.107256.
- Ricard, Y., L. Fleitout, and C. Froidevaux (1984), Geoid heights and lithospheric stresses for a dynamic Earth, *Annales Geophysicae*, 2, 267–286.
- Richards, F., M. J. Hoggard, S. Ghelichkhan, P. Koelemeijer, and H. Lau (2023), Geodynamic, geodetic, and seismic constraints favour deflated and dense-cored LLVPs, *Earth and Planetary Science Letters*, 602, 117964, doi: 10.1016/j.epsl.2022.117964.
- Richards, M. A., and B. H. Hager (1984), Geoid anomalies in a dynamic Earth, *Journal of Geophysical Research*, 89(B7), 5987–6002, doi: 10.1029/JB089iB07p05987.
- Rocchi, S., F. Storti, G. Di Vincenzo, and F. Rosetti (2003), Intraplate strike-slip tectonics as an alternative to mantle plume activity for the Cenozoic rift magmatism in the Ross Sea region, Antarctica, *Geological Society of London, Special Publications*, 210, 145–158, doi: 10.1144/GSL.SP.2003.210.01.09.
- Schaeffer, A., and S. Lebedev (2013), Global shear speed structure of the upper mantle and transition zone, *Geophysical Journal International*, 194, 417–449, doi: 10.1093/gji/ggt095.
- Seroussi, H., E. R. Ivins, D. A. Wiens, and J. Bondzio (2017), Influence of a West Antarctic mantle plume on ice sheet basal conditions, *Journal of Geophysical Research: Solid Earth*, 122(9), 7127–7155, doi: 10.1002/2017JB014423.
- Spasojevic, S., M. Gurnis, and R. Sutherland (2010a), Mantle upwellings above slab graveyards linked to the global geoid lows, *Nature Geoscience*, 3, 435–438, doi: 10.1038/ngeo855.
- Spasojevic, S., M. Gurnis, and R. Sutherland (2010b), Inferring mantle properties with an evolving dynamic model of the Antarctica-New Zealand region from the Late Cretaceous, *Journal of Geophysical Research*, 115, B05402, doi: 10.1029/2009JB006612.
- Steinberger, B. (2007), Effect of latent heat release at phase boundaries on flow in the Earth's mantle, phase boundary topography and dynamic topography at the Earth's surface, *Physics of the Earth and Planetary Interiors*, 164, 2–20, doi: 10.1016/j.pepi.2007.04.021.
- Steinberger, B. (2016), Topography caused by mantle density variations: observation-based estimates and models derived from tomography and lithosphere thickness, *Geophysical Journal International*, 205, 604–621, doi: 10.1093/gji/ggw040.
- Steinberger, B., and T. H. Torsvik (2010), Toward an explanation for the present and past locations of the poles, *Geochemistry, Geophysics, Geosystems*, 11, Q06W06, doi: 10.1029/2009GC002889.
- Steinberger, B., S. C. Werner, and T. H. Torsvik (2010), Deep versus shallow origin of gravity anomalies, topography and volcanism on Earth, Venus and Mars, 207, 564–577, doi: 10.1016/j.icarus.2009.12.025.
- Steinberger, B., W. Spakman, P. Japsen, and T. H. Torsvik (2015), The key role of global solid Earth processes in the late Cenozoic intensification of Greenland glaciation, *Terra Nova*, 27, 1–8, doi: 10.1111/ter.12133.
- Steinberger, B., C. P. Conrad, A. Osei Tutu, and M. J. Hoggard (2019), On the amplitude of dynamic topography at spherical harmonic degree two, *Tectonophysics*, 760, 221–228, doi: 10.1016/j.tecto.2017.11.032.
- Steinberger, B., S. Rathnayake, and E. Kendall (2021), The Indian Ocean Geoid Low at a plume-slab overpass, *Tectonophysics*, 817, 229037, doi: 10.1016/j.tecto.2021.229037.
- van der Wal, W., P. L. Whitehouse, and E. J. Schrama (2015), Effect of GIA models with 3D composite mantle viscosity on GRACE mass balance estimates for Antarctica, *Earth and Planetary Science Letters*, 414, 134–143, doi: 10.1016/j.epsl.2015.01.001.
- van der Wal, W., V. Barletta, G. Nield, and C. van Calcar (2022), Glacial isostatic adjustment and post-seismic deformation in Antarctica, *Geological Society of London, Memoirs*, 56, 315–341, doi: 10.1144/M56-2022-13.
- van Wyk de Vries, M., R. G. Bingham, and A. S. Hein (2018), A new volcanic province: an inventory of subglacial volcanoes in West Antarctica, *Geological Society of London, Special Publications*, 461, 231–248, doi: 10.1144/SP461.7.
- Weertman, J. (1974), Stability of the junction of an ice sheet and an ice shelf, *Journal of Glaciology*, 13, 3–11, doi: 10.3189/S0022143000023327.
- Wiens, D. A., W. Shen, and A. J. Lloyd (2021), The seismic structure of the Antarctic upper mantle, *Geological Society of London, Memoirs*, 56, 195–212, doi: 10.1144/M56-2020-18.